

UC Berkeley

UC Berkeley Electronic Theses and Dissertations

Title

Manipulating Light with Nano-Photonic Structures

Permalink

<https://escholarship.org/uc/item/7sj81748>

Author

Zeng, Bo

Publication Date

2015

Peer reviewed|Thesis/dissertation

Manipulating Light with Nano-Photonic Structures

By

Bo Zeng

A dissertation submitted in partial satisfaction of the

requirement for the degree of

Doctor of Philosophy

in

Physics

in the

Graduate Division

of the

University of California, Berkeley

Committee in charge:

Professor Feng Wang

Professor Michael Crommie

Professor Eli Yablonovitch

Fall 2015

Abstract

Manipulating Light with Nano-Photonic Structures

by

Bo Zeng

Doctor of Philosophy in Physics

University of California, Berkeley

Professor Feng Wang, Chair

Manipulation light in the nano scale, by controlling its phase or magnitude, is key to efficient and compact designs in modern photonic technology. Its application ranges from tele-communication, biological imaging to probing electronic phenomena and quantum computation. High Quality factor (Q) resonators for both dielectric and metallic devices with two dimensional form factors, and high on-off ratio wave modulators where light transmission can be tuned in situ are exemplary ideas and of great interest and importance in those applications. Among the light waves, terahertz radiation, known as the last frontier connecting microwave and optical regime in the electromagnetic spectrum, has been an increasingly active field of research. Recent development of THz sources and detection has led to an increasing demand of active devices for its wave manipulation. In the thesis, we focus our effort on developing novel nano photonic structures that act as better light modulator and resonators. We first develop theories regarding principles and

techniques to achieve tunable high Q resonances in dielectric photonic structures using a new “diatomic” design. The essence of the “diatomic” design is that it can dramatically improve Q of the resonating modes by minimizing the radiative far-field coupling. We then extend the concept of “diatomic” in dielectric gratings to “diatomic” metallic cavities that results in high Q plasmonic metamaterial resonators compared to conventional designs. Lastly, we demonstrate, in simulation and experiment, a hybrid metamaterial design showing much larger modulation power by combining metallic nano-slits with graphene, a promising THz-active 2D material. Our investigation into THz metamaterial designs combines device fabrication, numerical simulation, semi-analytical modelling and ultra-fast time domain THz measurements. Our theoretical and experimental results could provide insight to the physical understanding and future development of THz metamaterial devices, as well as being of value to the THz community that seeks application with high performance modulator/resonators in general.

TABLE OF CONTENTS

List of Figures	iii
Acknowledgement	iv
Introduction.....	vi
1 FDTD and RCWA	1
1.1 Introduction to FDTD.....	1
1.1.1 FDTD for 1D and 2D Problems.....	2
1.1.2 FDTD with dielectric functions	5
1.1.3 Boundary Conditions	8
1.2 Introduction to RCWA.....	9
1.2.1 Eigenmode inside gratings.....	10
1.2.2 Matching the boundary condition.....	12
1.2.3 Far field reflection and transmission.....	13
2 Broadband THz Modulators by Graphene-Metamaterial Hybrid Device.....	14
2.1 Motivation	14
2.2 Recent Progress	15
2.3 Theory	16
2.3.1 Far Field Transmission of Metamaterial.....	16
2.3.2 Local Field Enhancement	20
2.4 Experiment	23
2.4.1 Device Fabrication	23
2.4.2 Conductivity of graphene sheet in the slit.....	24
2.4.3 Measuring THz transmission	26
2.5 Conclusion.....	28
3 Tunable dark modes in one-dimensional “diatomic” dielectric gratings.....	29
3.1 Motivation	29
3.2 Theory	30
3.2.1 Dark modes in grating.....	30
3.2.2 Zone folding.....	31
3.2.3 Diatomic structures	33
3.3 Simulation	34
3.3.1 Q factor of dark mode resonance	34

3.3.2	Interaction between bright and dark eigenmodes	35
3.3.3	A representative design.....	37
3.3.4	In situ tunable resonator: a possible application	39
3.4	Summary	40
4	High Q metallic resonators using diatomic designs.....	42
4.1	Motivation	42
4.2	Theory	43
4.2.1	MDM waveguide	43
4.2.2	MDM cavity and its resonance	45
4.2.3	Reflectivity at the Air-Cavity interface.....	46
4.2.4	MDM diatomic gratings.....	48
4.2.5	Coupling between adjacent MDM cavities.....	48
4.2.6	Effective Fabry-Perot and Critical Coupling	52
4.3	Simulation	54
4.3.1	Q factors of dark modes.....	54
4.3.2	Critically coupling design curves.....	55
4.3.3	An ultra-high Q metallic cavity resonator	56
4.4	Conclusion.....	57
	References.....	58

LIST OF FIGURES

Figure 1-1: Two dimensional FDTD calculation grids for a TM wave.....	3
Figure 1-2: Typical field expansion of RCWA of one dimensional gratings.....	9
Figure 2-1: Broadband Terahertz metamaterial of periodic gold slits.....	17
Figure 2-2: Schematic representation of a Faraday Loop (A-B-C-D).	18
Figure 2-3: Electrical transport characterization and the THz transmission modulation.	25
Figure 2-4: THz modulation by the graphene/metamaterial hybrid device.....	26
Figure 2-5: THz modulation depth vs. graphene conductivity.	27
Figure 3-1: Design of the Double Bump and the emergence of intrinsic “dark” modes.	32
Figure 3-2: Dependence of Q on filling factors for the “diatomic” design	34
Figure 3-3: Demonstration of the effect of filling factors on the double bump design.	36
Figure 3-4: The design of a typical single high Q resonance in “diatomic” grating.	37
Figure 3-5: In-situ tuning of the high Q resonance in “diatomic” gratings	39
Figure 4-1: A typical MDM configuration with dielectric width d	43
Figure 4-2: Field distribution for the symmetric H_z TM mode.....	44
Figure 4-3: A MDM cavity and field distribution E_x at one of its resonance.....	45
Figure 4-4: MDM cavities in a grating.	47
Figure 4-5: Diatomic design for MDM gratings.....	48
Figure 4-6: An iterative algorithm to calculate κ, r_1, r_2 in a self-consistent way.....	51
Figure 4-7: Phase of both $\kappa -$ and $\kappa +$ in the design parameter space	54
Figure 4-8: Q factors of cavity for both $\kappa -$ and $\kappa +$ in the design parameter space.....	55
Figure 4-9: Impedance matching design curve.	55
Figure 4-10: A representative diatomic MDM cavity design with critically coupling.....	56

ACKNOWLEDGEMENT

I would like to first express my appreciation to my advisor Prof. Feng Wang for his choice of letting me join the group, despite the fact that I came from an engineering background and was then only new to physics. He has introduced me to the world of graphene, THz and quantitative modeling. For the years to come, his clarity in analogy yet conciseness of mind is the most enlightening. And he has helped me steer all the way toward graduation. All in all, I am in great debt to his generosity, kindness and invaluable help. Working with Feng has been a unique and irreplaceable part of my life.

I am also deeply grateful to many of my colleagues in the group. Sufei Shi and Huiling Han have helped me not only by generously sharing their knowledge but lending me courage and strength during the hard time of the one-year spree of THz experiments, when I was often at lost. Most of the time we felt like a family: we share our vastly different personal stories when we are free, and might have argued for plans on experiments, but at the end of the day we get united to work. I should thank them for showing me optimism in many of the difficult times.

Zhiwen Shi and I shared a lot interest in science and personal hobbies that we ended up conducting AFM experiments together. I've learned a lot from him, his perseverance and devotion into science in particular. He would be a life-long friend of me. I would like to give him best wishes for his career as a professor in SJTU.

I also have had collaboration with Baisong Geng in my first years for graphene growth and transfer, Lili Jiang for the AFM near field measurements and Arka Majumdar for his help with nonlinear spectroscopy and device fabrication. Arka's help with career advice and recommendation for internship to Google X labs is invaluable. He has been a sincere friend of mine despite that we only worked together for one year in the group, after which he soon became a Professor in UW.

Among others, Kaihui Liu, Long Ju, Tsung-Ta Tang, Xiaoping Hong, Jason Horng, Jonghwan Kim, Steve Byrnes, Yaqing Bie, Chenhao Jin are great lab-mates working with whom I always enjoyed.

Finally, I would like to thank Anne Takizawa and Anthony Vitan in our department for their support in the 5 years. Anne solved many of my problems in terms of classes, careers beyond academia and GSI choices throughout the PhD program. Without Anthony, some of our lab's renovation that is necessary for the experiment to run would not be possible.

INTRODUCTION

1. Metamaterial and its optical resonance

Metamaterial is an umbrella word for man-made materials whose electric and magnetic properties can be readily engineered¹. Examples that demonstrate its exotic properties include negative refractive index lenses, invisible cloaks and so on^{2,3}. Metamaterial is usually composed of periodic structures of subwavelength size, where the detail of each unit cell is too small to be “seen” from the incident light. Therefore, the entire metamaterial, however complex in its unit cells, can be modelled as an equivalent bulk whose permittivity ϵ and permeability μ are convenient functions of some design parameters⁴.

Generally speaking, properties of a metamaterial are controlled by its constituting unit cells, and its periodic nature makes its optical eigenstates Bloch waves. There are numerous ways to study the optical behavior of a metamaterial from its unit cells, either through LC circuit modelling⁵, parameter extraction from S Matrix⁶ in numerical simulations or by semi-analytic methods like Rigorous Coupling Wave Analysis (RCWA) and moment matching^{7,8}. We focus on semi-analytic methods in this thesis when we deal with metamaterial designs.

Among many of the variants of metamaterial, metasurface is a particular type with extremely thin optical thickness. Apart from being a conventional metamaterial, metasurface holds the advantage of easy integration with other 2D materials (graphene/MoS₂) as a possible experiment platform as well as large fabrication throughputs, i.e. using lithography, thanks to its planar geometry.

By engineering the real part of ϵ , it is possible to make metasurface support reflection or transmission resonances around the wavelength of interest. By engineering the imaginary part of

ϵ , we can further control the Quality factor (Q). Also known as “scale invariance”, a design of metamaterial for one wavelength can be relatively easily applied to a different range of wavelengths just by scaling the design parameters accordingly. This attribute is practically invaluable as it makes validating optical metamaterial designs much easier. Experiments can potentially be done in the THz or even microwave regime to verify optical designs using devices with μm features instead those of nms.

2. Graphene and its free carrier THz Absorption

Graphene, a two dimensional sheet of carbon atoms arranged in a honeycomb lattice, has been an important example of two dimensional (2D) materials. Band structure of graphene calculated using tight binding models reveals that it a semi metal and it has a linear $\omega - k$ dispersion curve for the so called “massless fermions” around $K(K')$ points in the Brillouin zone. The most significant optical and electronic consequences of this is the uniform absorption in the long wavelength regime⁹ and efficient tuning of Fermi levels by electrostatic gating¹⁰.

Dielectric functions of graphene have been studied in theory¹¹ and in experiments¹² in depth. It follows that the dielectric function approximates a Drude response in the long wavelength limit, indicating a dominant contribution from free carriers. Therefore, we can engineer its dielectric function by controlling the free carrier concentration, also known as Drude weight¹³. Thanks to the low density of states (DOS) near its $K(K')$ point, it is remarkably efficient to dope graphene using simple electrostatic gating, for example, using ion gel¹².

We will primarily use this technique to tune the Fermi level of our graphene devices in experiments described in this thesis.

3. Simulation Techniques: Numerical and Semi-Analytical Methods

Simulation is, at the expense of computational resources (memory, CPU, network etc.), a general purpose and vastly powerful tool to solve electromagnetic problems in complex systems. Capable of computing the distribution and dynamics for electromagnetic fields, it often lends insight to various optical systems like plasmonic gratings and resonating cavities. Simulation using numerical methods largely comes into two flavors: FDTD (Finite Difference Time Domain) and FEM (Finite Element Method)^{14,15}. In a nutshell, they tackle the problem by mapping E and H fields into space-time grids and search for solution in each grid iteratively, following the form of discretized Maxwell equations. While FDTD is capable of simulating a broadband source and visualizing the field evolution with time, FEM has advantages of supporting more complex, non-uniform grids as well as faster computation for high Q modes, where the former generally fall short of.

Numerical simulation is a brutal force solver for Maxwell equations, as it doesn't assume any prior knowledge on the form of its solutions. When it does, however, computational costs can be drastically reduced. RCWA (Rigorous Coupling Wave Analysis)¹⁶ is such an example that assumes a planar wave excitation and planar wave solutions in the far field. It is a semi-analytic method as it involves analytical forms of eigenmodes in incidence (region I), device (region II) and transmission (region III). It expands the field in all three regions into their corresponding, orthonormal eigenmodes and match the boundary condition to solve for respective coefficients. Its computational speed can improve as we truncate higher order eigenmodes, and from the convergence curve we can gain insight on which eigenmodes the observed resonance is mostly attributed to.

1 FDTD AND RCWA

1.1 INTRODUCTION TO FDTD

FDTD (Finite Difference Time Domain) method is, in a broad language, a family of appropriate algorithms that predicts the time and space evolution of electromagnetic fields with high numerical accuracy for any given configuration. The configuration, in electromagnetic languages, is the geometric arrangement of permittivity (ϵ) and permeability (μ) plus any source setup if incident waves are involved. FDTD always assumes no free charge for Gauss's Law, hence:

$$\nabla \cdot \vec{D} = 0 \quad (1 - 1)$$

$$\nabla \cdot \vec{B} = 0 \quad (1 - 2)$$

Recall Maxwell Equations for Ampere's and Faraday's law in free space:

$$\nabla \times \vec{E} = -\frac{\partial \vec{B}}{\partial t} \quad (1 - 3)$$

$$\nabla \times \vec{H} = \epsilon_0 \frac{\partial \vec{E}}{\partial t} \quad (1 - 4)$$

FDTD can be written using staggered update rules for both 1D and 2D problems in a discretized space and time scheme. The staggering is necessary to make sure FDTD's numerical stability, ensuring a conservation of electro-magnetic energy to avoid blow up for either \vec{E} or \vec{B} fields after several rounds of updates.

1.1.1 FDTD for 1D and 2D Problems

For 1D case, let \vec{E} be polarized in y , \vec{B} be polarized in z , and our 1D system in along x axis, Eq. (1-3) and (1-4) can be rewritten symmetrically:

$$\frac{\partial E_y}{\partial t} = -\frac{1}{\epsilon_0} \frac{\partial H_z}{\partial x} \quad (1-5)$$

$$\frac{\partial H_z}{\partial t} = -\frac{1}{\mu_0} \frac{\partial E_y}{\partial x} \quad (1-6)$$

Take the central difference approximations for both space and time derivatives and we will have a finite difference form:

$$\frac{E_y^{t+0.5\delta t}(x) - E_y^{t-0.5\delta t}(x)}{\delta t} = -\frac{1}{\epsilon_0} \frac{H_z^t(x + 0.5\delta x) - H_z^t(x - 0.5\delta x)}{\delta x} \quad (1-7)$$

$$\frac{H_z^{t+\delta t}(x + 0.5\delta x) - H_z^t(x + 0.5\delta x)}{\delta t} = -\frac{1}{\mu_0} \frac{E_y^{t+0.5\delta t}(x + \delta x) - E_y^{t+0.5\delta t}(x)}{\delta x} \quad (1-8)$$

Eq. (1-7) is following the exact central difference formalism while Eq. (1-8) has a grid shift of $0.5\delta x$ and $0.5\delta t$ for both H_z and E_y . Rearranging Eq. (1-7) and Eq. (1-8), it is possible to write a set of temporal update equations for $E_y(x), H_z(x)$ in the entire problem space, giving FDTD the name “time domain”:

$$E_y^{t+0.5\delta t}(x) = E_y^{t-0.5\delta t}(x) - \frac{\delta t}{\epsilon_0 \delta x} (H_z^t(x + 0.5\delta x) - H_z^t(x - 0.5\delta x)) \quad (1-9)$$

$$H_z^{t+\delta t}(x + 0.5\delta x) = H_z^t(x + 0.5\delta x) - \frac{\delta t}{\mu_0 \delta x} (E_y^{t+0.5\delta t}(x + \delta x) - E_y^{t+0.5\delta t}(x)) \quad (1-10)$$

Eq. (1-9), Eq. (1-10) moves both E_y and H_z in time by step of δt . It is important to note the update equations are written in a staggered manner. As an example, in order to calculate an update for E_y

at position x from time stamp t_A to t_B , we use fields of H_z at staggered positions x_A and x_B calculated at time stamp in the middle of t_A and t_B . So that $t = (t_A + t_B)/2$, also $x = (x_A + x_B)/2$. The same rule applies for H_z . In this way, we always calculate E at odd $(1/2)\delta t$ time stamps, and H in even time stamps. Similarly, we always calculate H at odd $(1/2)\delta x$ space coordinates, and E at even coordinates. This interleaving manner ensures a controlled pace at which the two mutually interacting components updates, and also avoids blow off instabilities should an update cycle emerges.

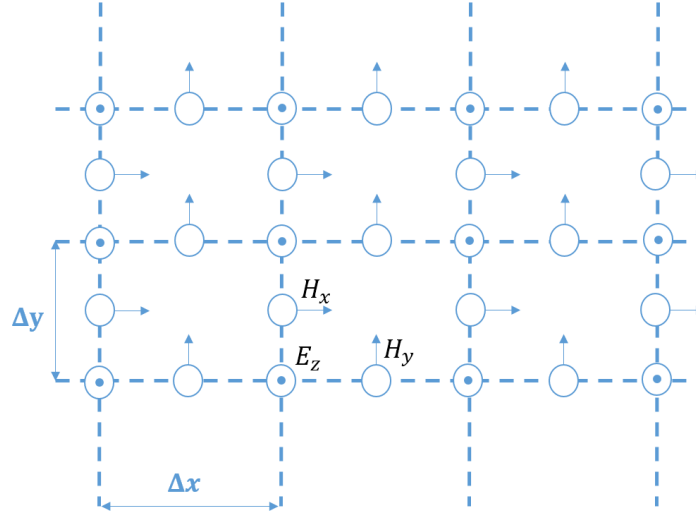


Figure 1-1: Two dimensional FDTD calculation grids for a TM wave

To make Eq. (1-9) and Eq. (1-10) more symmetric, it is customary to normalize E so that $\tilde{E} = \sqrt{\epsilon_0/\mu_0} E$. Using this notation, Eq. (1-9) and Eq. (1-10) become:

$$\tilde{E}_y^{t+0.5\delta t}(x) = \tilde{E}_y^{t-0.5\delta t}(x) - \frac{\delta t}{\sqrt{\epsilon_0\mu_0}\delta x} (H_z^t(x + 0.5\delta x) - H_z^t(x - 0.5\delta x)) \quad (1 - 11)$$

$$H_z^{t+\delta t}(x + 0.5\delta x) = H_z^t(x + 0.5\delta x) - \frac{\delta t}{\sqrt{\epsilon_0\mu_0}\delta x} (\tilde{E}_y^{t+0.5\delta t}(x + \delta x) - \tilde{E}_y^{t+0.5\delta t}(x)) \quad (1 - 12)$$

Note the time domain update step δt cannot be too large or it will connect spacelike points in space-time, which violates special relativity. To enforce the compliance, we set $\frac{\delta t}{\delta x} < \frac{1}{c}$, where δx is the maximum sampling step in all space dimensions. In general, for a N dimensional problem, we need $\frac{\delta t}{\delta x} < \frac{1}{\sqrt{N}c}$. Since all physical problems occur within 3D, it is sufficient to set $\frac{\delta t}{\delta x} = \frac{1}{2c}$. This is also known as the Courant condition^{17,18} in FDTD. On the other hand, δx is referred to as the spatial sampling size. It is a rule of thumb that we set $\delta x \leq \lambda/10$ to obtain numerically accurate and stable solutions. It is in tandem with experience that one needs roughly 10 sampling points to resolve a sinusoidal curve within one cycle.

FDTD can readily solve for 2D electromagnetic problems using central difference time domain equations generalized from the above 1D cases. For a TM mode where only H_x, H_y, E_z are nonzero, the update equations can be written similarly as:

$$\begin{aligned} \frac{\tilde{E}_z^{t+0.5\delta t}(x, y) - \tilde{E}_z^{t-0.5\delta t}(x, y)}{\delta t} &= \frac{1}{\sqrt{\epsilon_0\mu_0}} \left(\frac{H_y^t(x + 0.5\delta x, y) - H_y^t(x - 0.5\delta x, y)}{\delta x} \right) \\ &\quad - \frac{1}{\sqrt{\epsilon_0\mu_0}} \left(\frac{H_x^t(x, y + 0.5\delta y) - H_x^t(x, y - 0.5\delta y)}{\delta y} \right) \end{aligned} \quad (1 - 13)$$

$$\begin{aligned} &\frac{H_x^{t+\delta t}(x, y + 0.5\delta y) - H_x^t(x, y + 0.5\delta y)}{\delta t} \\ &= -\frac{1}{\sqrt{\epsilon_0\mu_0}} \frac{\tilde{E}_z^{t+0.5\delta t}(x, y + \delta y) - \tilde{E}_z^{t+0.5\delta t}(x, y)}{\delta y} \end{aligned} \quad (1 - 14)$$

$$\begin{aligned}
& \frac{H_y^{t+\delta t}(x + 0.5\delta x, y) - H_y^t(x + 0.5\delta x, y)}{\delta t} \\
&= -\frac{1}{\sqrt{\epsilon_0\mu_0}} \frac{\tilde{E}_z^{t+0.5\delta t}(x + \delta x, y) - \tilde{E}_z^{t+0.5\delta t}(x, y)}{\delta x} \tag{1-15}
\end{aligned}$$

Note it is possible to have independent sampling sizes for x and y . A familiar staggering manner follows from the 1D case and we can then write the time stamp update equations for \vec{E} and \vec{H} correspondingly. In our work, we mostly use 2D FDTD simulations. For people interested in 3D and more complex formalism, they can refer to Kane Yee's seminar paper¹⁹, where a structure called Yee's cell is employed.

1.1.2 FDTD with dielectric functions

Free space FDTD provides a trivial solution to Maxwell Equations. In problems of interest, however, materials with frequency-dependent dielectric functions are usually present, giving rise to complex electromagnetic phenomena. Assuming they are all non-magnetic (keeping $\mu_r = 1$), FDTD formalism needs certain adjustment to get compatible with these materials.

The first, simpler example would be to incorporate a material with dielectric constant $\epsilon_r(x, y)$ in our simulation. To do so, we need to recognize the general form of Ampere's Law and replace \tilde{E} by \tilde{D} in its central difference equation. Note that $\epsilon_r \tilde{E} = \tilde{D}$, therefore we update $\frac{1}{\sqrt{\epsilon_0\mu_0}}$ with

$\frac{1}{\epsilon_r(x,y)\sqrt{\epsilon_0\mu_0}}$ in Eq. (1-10) and Eq. (1-12). This is consistent with free space formalism where

$$\epsilon_r(x, y) = 1.$$

We will then use metal (or to a larger extent, plasma) as our second and more general example.

The dielectric function is now frequency dependent.

$$\epsilon_r(\omega) = 1 + \frac{\omega_p^2}{\omega(j\nu_c - \omega)} \quad (1 - 16)$$

where ω_p is the plasma frequency, ν_c is the collision frequency for a given metal.

Ampere's law still holds for \vec{D} but the simple connection with $\vec{D} = \epsilon_r \vec{E}$ in time domain breaks down. They are now connected in time domain with a full convolutional relation as follows:

$$\vec{D}(t) = \int_{\tau=-\infty}^t \epsilon(t - \tau) \vec{E}(\tau) \quad (1 - 17)$$

where $\epsilon(t)$ and $\epsilon(\omega)$ are related by Inverse Fourier Transform:

$$\epsilon_r(t) = \int_{-\infty}^{\infty} \epsilon_r(\omega) e^{i\omega t} d\omega \quad (1 - 18)$$

The trick employed in the simple constant dielectric case will fail as $D(t)$ is calculated by not the instantaneous $E(t)$ but its past values back to the beginning of simulation. We therefore need a better machinery to find out update equations from \vec{D} to \vec{E} .

It turns out that Z transform is the ideal tool to convert frequency domain to finite difference domain without dealing with complicated algebra in the convolution²⁰. From the constitutional law:

$$\begin{aligned} \vec{D}(\omega) &= \epsilon_r \vec{E}(\omega) = \left(1 + \frac{\omega_p^2}{\omega(j\nu_c - \omega)} \right) \vec{E}(\omega) \\ &= \left(1 + \frac{\omega_p^2}{\nu_c} \frac{1}{j\omega} - \frac{\omega_p^2}{\nu_c} \frac{1}{\nu_c + j\omega} \right) \vec{E}(\omega) \end{aligned} \quad (1 - 19)$$

Applying Z transform in both sides:

$$\vec{D}(z) = \left(1 + \frac{\omega_p^2 \delta t / v_c}{1 - z^{-1}} - \frac{\omega_p^2 \delta t / v_c}{1 - e^{-v_c \delta t} z^{-1}} \right) \vec{E}(z) \quad (1 - 20)$$

Rearrange and let $S(z) = \frac{\omega_p^2 \delta t}{v_c} \left(\frac{1 - e^{-v_c \delta t}}{1 - (1 - e^{-v_c \delta t})z^{-1} + e^{-v_c \delta t} z^{-2}} \right) E(z)$ be an auxiliary function, we have:

$$E(z) = D(z) - z^{-1}S(z) \quad (1 - 21a)$$

$$\begin{aligned} S(z) &= (1 + e^{-v_c \delta t})z^{-1}S(z) - e^{-v_c \delta t}z^{-2}S(z) \\ &+ \frac{\omega_p^2 \delta t}{v_c} (1 - e^{-v_c \delta t})E(z) \end{aligned} \quad (1 - 21b)$$

We have thus established the update formula for E from D . Rewrite this Z form into time domain, we have the following set of update rules (assuming a 2D problem with TM mode):

$$E_z^t(x, y) = D_z^t(x, y) - S_z^{t-\delta t}(x, y) \quad (1 - 22a)$$

$$\begin{aligned} S_z^t(x, y) &= (1 + e^{-v_c \delta t})S_z^{t-\delta t}(x, y) - e^{-v_c \delta t}S_z^{t-2\delta t}(x, y) \\ &+ \frac{\omega_p^2 \delta t}{v_c} (1 - e^{-v_c \delta t})E_z^t(x, y) \end{aligned} \quad (1 - 22b)$$

where $E(t)$ is updated from $D(t)$ minus the auxiliary function at last time stamp $S(t - \delta t)$, and $S(t)$ is updated according using its own history of previous two time stamps. Collision frequency v_c here is physically depicted as a decaying factor for connecting quantities several time stamps older.

Adding Eq. (1-22) to Eq. (1-13), (1-14), (1-15) and replacing \vec{E} with \vec{D} , we arrive at the final formula for running FDTD in a system with dielectric and metal. In general, material with arbitrary dielectric function $\epsilon(\omega)$ can be transformed to Z forms and the above formalism still applies, including Debye terms for a conductor, as well as Lorentian terms for materials with a absorption peak. This completes an overall setting for our study with metamaterials using FDTD.

1.1.3 Boundary Conditions

Boundaries are important concepts as we use FDTD to simulate larger and larger problems. For one thing, we barely care about solutions outside areas of our interest in the problem. In such cases, we want to simulate only this particular area for economic reasons and a special type of boundary is necessary to enclose the area and truncate outgoing fields without disturbing solutions inside.

For another, we want to make full use of available symmetries in our problem, so that the computational power required for solution is drastically reduced. A prominent example is grating, where discrete translational symmetry is present. It is sufficient to simulate a unit cell of the grating with periodic conditions, which imposes certain rules to fields at cell boundaries.

The first type is called a Perfectly Matching Layer (PML) boundary²¹. It mimics, as its name indicates, a layer with perfectly matched impedance so that any wave incident to it from the simulated area will transmit through and incrementally dissipated. It ensures no reflection happens at its interface with the simulated area so our solution is not disturbed. By employing PML, we can efficiently simulate a limited region of area that we are interested in while solutions outside of this area are safely thrown away.

The second type of FDTD boundaries is called the periodic boundary. It is equivalent to imposing a set of mathematical constraints at the specified coordinates. In the context of a one dimensional

(1D) grating, periodic boundaries at $x = 0, x = L$ is implemented as $E(0) = E(L)e^{ik_x L}, H(0) = H(L)e^{ik_x L}$, where L is the size of grating unit cells and k_x is Bloch vector in reduced Brouillon zone. This formalism can be conveniently extended to 2D and 3D cases.

1.2 INTRODUCTION TO RCWA

RCWA is a semi-analytic method in the frequency domain that takes advantage of eigenmode expansion to obtain far field solutions of a layered system.

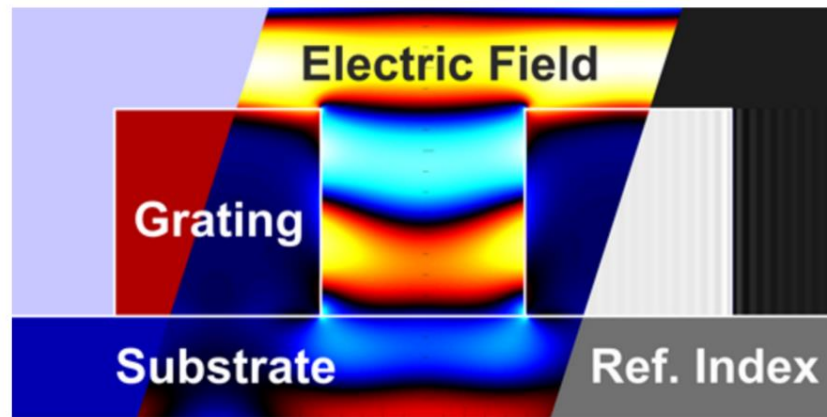


Figure 1-2: Typical field expansion of RCWA of one dimensional gratings

source: <http://www.photon.com>.

It is useful, for example, to calculate reflection/transmission spectra of a grating. It is generally faster compared to FDTD as it converts the problem of calculating the full electromagnetic fields in time domain to coefficients of electromagnetic eigenmodes in the frequency domain. It is also particularly suited for resonating systems, since its computational time is independent of Quality factor (Q) of the resonance and its frequency resolution can be extremely high, which usually means protracted simulation time in FDTD.

1.2.1 Eigenmode inside gratings

An efficient representation of eigenmodes in a uniform medium are planar waves. It is widely used in RCWA on the incidence and transmission side for its simple forms, where a substrate with constant dielectric function (or free space) is employed. In Fig. 1-2, the device layer (layer II, the layer of grating) is usually where interesting optical phenomena arise. If layer II is a dielectric slab, its eigenmodes will be trivial planar waves and our problem is reduced to a simple F-P cavity. On the other hand, if layer II is of a more complex structure, then the spatial profile of its leading eigenmodes, together with their relative phases, will eventually determine the overall far field optical spectrum of the device. Let's use a binary rectangular grating as an example.

Inside a binary rectangular grating, the dielectric function $\epsilon(x)$ is piecewise of the form

$$\begin{aligned}\epsilon(x) &= \epsilon_1, 0 < x \leq s \\ \epsilon(x) &= \epsilon_2, s < x \leq D\end{aligned}\tag{1 - 23}$$

In a unit cell (one period), we can write its eigensolutions in these two regions^{22s}. Without loss of generality, we consider a TM mode. In region I, Electrical field E_y can be represented, in the frequency domain, as sum of left and right propagating fields, with complex amplitudes E_1^+, E_1^- to be determined:

$$E_y^I(x) = E_1^+ e^{-jk_1x} + E_1^- e^{jk_1x}\tag{1 - 24a}$$

Accordingly, by Faraday's law, we can get $H_z^I(x)$ as:

$$H_z^I(x) = \frac{\omega\epsilon_1}{k_1} (E_1^+ e^{-jk_1x} - E_1^- e^{jk_1x})\tag{1 - 24b}$$

where $k_1 = \sqrt{k_0\epsilon_1^2 - \beta^2}$, and β is the propagation constant for the eigenmodes in z direction.

In fact, the amplitudes E_1^+ and E_1^- are determined by values of $E_y^I(0)$ and $H_z^I(0)$, by setting $x = 0$ of Eq. (1-24).

$$E_1^+ = \frac{1}{2} \left(E_y^I(0) + \frac{k_1}{\omega \epsilon_1} H_z^I(0) \right) \quad (1-25a)$$

$$E_1^- = \frac{1}{2} \left(E_y^I(0) - \frac{k_1}{\omega \epsilon_1} H_z^I(0) \right) \quad (1-25b)$$

Substitute Eq. (1-25) back to Eq. (1-24), we obtain a characteristic matrix concerning field propagation relations from $x = 0$ in region I:

$$\begin{aligned} \begin{bmatrix} E_y^I(x) \\ H_z^I(x) \end{bmatrix} &= \begin{bmatrix} \cos k_1 x & -j \frac{k_1}{\omega \epsilon_1} \sin k_1 x \\ -j \frac{\omega \epsilon_1}{k_1} \sin k_1 x & \cos k_1 x \end{bmatrix} \begin{bmatrix} E_y^I(0) \\ H_z^I(0) \end{bmatrix} \\ &= T(k_1, x) \begin{bmatrix} E_y^I(0) \\ H_z^I(0) \end{bmatrix} \end{aligned} \quad (1-26)$$

Similarly, we write the characteristic matrix for region II:

$$\begin{aligned} \begin{bmatrix} E_y^{II}(x) \\ H_z^{II}(x) \end{bmatrix} &= \begin{bmatrix} \cos k_2(x-s) & -j \frac{k_2}{\omega \epsilon_2} \sin k_2(x-s) \\ -j \frac{\omega \epsilon_2}{k_2} \sin k_2(x-s) & \cos k_2(x-s) \end{bmatrix} \begin{bmatrix} E_y^{II}(s) \\ H_z^{II}(s) \end{bmatrix} \\ &= T(k_2, x-s) \begin{bmatrix} E_y^{II}(s) \\ H_z^{II}(s) \end{bmatrix} \end{aligned} \quad (1-27)$$

Matching the continuity boundary condition at $x = s$, we have:

$$\begin{bmatrix} E_y^{II}(x) \\ H_z^{II}(x) \end{bmatrix} = T(k_2, x-s) T(k_1, s) \begin{bmatrix} E_y^I(0) \\ H_z^I(0) \end{bmatrix} \quad (1-28)$$

In particular, set $x = D$:

$$\begin{bmatrix} E_y^{II}(D) \\ H_z^{II}(D) \end{bmatrix} = T(k_2, D - s)T(k_1, s) \begin{bmatrix} E_y^I(0) \\ H_z^I(0) \end{bmatrix} = e^{\pm ikD} \begin{bmatrix} E_y^I(0) \\ H_z^I(0) \end{bmatrix} \quad (1 - 29)$$

e^{ikx} is determined by the incident condition, and it relates relative phases between adjacent unit cells. In the case of normal incidence, $e^{ikx} = 1$.

Eq. (1-29) is recognized as a eigenvalue-eigenvector function for matrix $T(k_1, k_2, D, s) = T(k_2, D - s)T(k_1, s)$. Relating $tr(T)$ to the sum of its eigenvalues, a dispersion equation for propagating modes in the grating region can be established:

$$\cos kD = \cos k_1 s \cos k_2 (D - s) - \frac{1}{2} \left(\frac{\epsilon_1 k_2}{k_1 \epsilon_2} + \frac{\epsilon_2 k_1}{k_2 \epsilon_1} \right) \sin k_1 s \sin k_2 (D - s) \quad (1 - 30)$$

Given k from incident conditions, Eq. (1-30) is an equation relating ω with propagation constant β , as $k_i = \sqrt{\epsilon_i \omega^2 / c^2 - \beta^2}$ for $i = 1, 2$. This formalism can be easily extended to unit cells with 3 or more regions (beyond binary gratings).

Once β is solved from Eq. (1-9), k_1, k_2 will be determined and so is shape of each eigenmode. Usually for each ω , there are multiple solutions for β . They are arranged with ascending $|k_i|$.

Note that some of the modes are even (bright), some of the modes are odd (dark). Their overlap with free space fields determine their coupling coefficient to the fat field. The concept of bright and dark modes inside grating can be useful when we study optimizing gratings for large Q factors.

1.2.2 Matching the boundary condition

To solve r_m, t_m and mode coefficients inside the grating region, we need to additional constraints. Physically speaking, we need to match E and H according to Maxwell's Equations at both the incidence and transmission boundaries ($y = 0, y = t$, where t is the thickness of the grating).It

yields a set of simultaneous equations that one can solve numerically. A full treatise of the topic in matrix forms can be found in references elsewhere^{16,23}.

1.2.3 Far field reflection and transmission

Once r_m, t_m are solved and repeated for many different wavelengths, we are able to calculate reflection and transmission spectra. For a system with many nonzero r_m (or t_m), each of them corresponds to a diffraction term in the far field. For a subwavelength grating where $D \ll \lambda$, only zeroth order reflection/transmission is non-evanescent. In such cases, we can simply get:

$$R = |r_0|^2, T = |t_0|^2$$

Below is an example of spectra calculated using RCWA compared to FDTD. They agree with each other very well. By RCWA, we can further inspect the field distribution on and off resonance, to validate our intuition of the origin of such resonances.

2 BROADBAND THZ MODULATORS BY GRAPHENE-METAMATERIAL HYBRID DEVICE

2.1 MOTIVATION

Terahertz (THz) wave is widely referred to as the “last frontier”²⁴ in the electromagnetic spectrum, with frequency ranging from 0.3 to 10 THz (1 THz = 10^{12} Hz) and photon energy on the order of several meV. THz technology has been widely recognized as a promising candidate for next generation imaging and wireless communication. Although it is still not mature compared to its electronic and optical counterparts, we have seen significant progress in THz generation^{25,26,27} and detection^{28,29} over the last decade. Consequently, demand for active THz wave control is surging. Among them, electrically controlled THz modulator is particularly appealing because it provides both real time manipulation of THz wave and easy integration on chip.

Research on electrical modulation of THz waves has been an increasingly active field lately. Graphene, in particular, has been shown to provide an impressive broadband modulation of ~ 20% on power³⁰, a significant improvement over previous semiconductor modulators. This broadband modulation is of special advantage given the limited THz sources available. At the same time, the modulation depth of THz waves is still limited by the finite conductivity achievable for a single atomic layer. Alternatively, coupling semiconductor or graphene to a resonant THz meta-material results in a larger modulation depth but it only works for a narrow band frequency window^{31,32}.

2.2 RECENT PROGRESS

Compared to a plain sheet of graphene, plasmonic structures exhibit extraordinary light transmission and greatly enhanced local electrical field^{33,34}. By modifying this enhanced field, it is possible to achieve large modulation of transmitted waves. Atomically thin and flexible, graphene can efficiently couple to locally enhanced fields, known as “hot spots”. Consequently we can achieve large modulation with a graphene/plasmonic-structure hybrid device using graphene as an active load^{35,36}.

However, there remain two major challenges to implement graphene/plasmonic-structure hybrid device for optimized THz modulation. First of all, it is desirable to preserve the broadband THz modulation of bare graphene for the new hybrid device³⁰. Secondly, an efficient coupling between graphene and the plasmonic structure is necessary for optimized modulation. For example, graphene conductivity is attributed to the delocalized π -electrons so that the enhanced local field needs to be engineered “in-plane” to maximize the coupling efficiency. Recently, semiconductors³⁷ or graphene^{31,32} coupled to resonant THz metamaterials have shown improved modulation depth but they only work for a narrow frequency window. Meanwhile, researchers have attempted to improve the THz modulation by coupling graphene to broadband metamaterials³⁸, but the modulation depth is still limited and the study on optimized coupling is lacking.

2.3 THEORY

2.3.1 Far Field Transmission of Metamaterial

A meta-material surface made of periodic gold slit arrays, shown schematically in Fig. 2-1a, is used in our design to enhance THz modulation. It has been shown previously³⁹ that a single sub-wavelength slit of width w , light with polarization perpendicular to the slit (along x axis) excites surface current that induces charge oscillations across the slit. This capacitive-coupled oscillation gives rise to a near field enhancement factor of $\sim\lambda/w$ in the slit according to the effective λ -zone theory⁴⁰, and the transmission through the slit comes from the displacement current in the slit. On the contrary, periodic gold slits exhibit a wavelength independent enhancement factor of $\sim p/w$ in the slit if $p \ll \lambda$, while the enhancement reduces to the single slit case ($\sim\lambda/w$) if $p \sim \lambda$. In the $p \ll \lambda$ limit, we expect that the radiation from each periodic slit adds up coherently, giving rise to a large THz transmission.

In the coordinate system shown in Fig. 2-2, $z = 0$ denotes the interface between the slit array and medium on the transmission side. To relate electrical fields in both regions, we apply the tangential continuity boundary condition from Faraday's Law at the interface:

$$E_x^{III}(x, z = 0) = E_x^{II}(x, z = 0) \quad (2 - 1)$$

where $E_x^I(x, z)$, $E_x^{III}(x, z)$ is the x component of Electric field in region I and region III respectively.

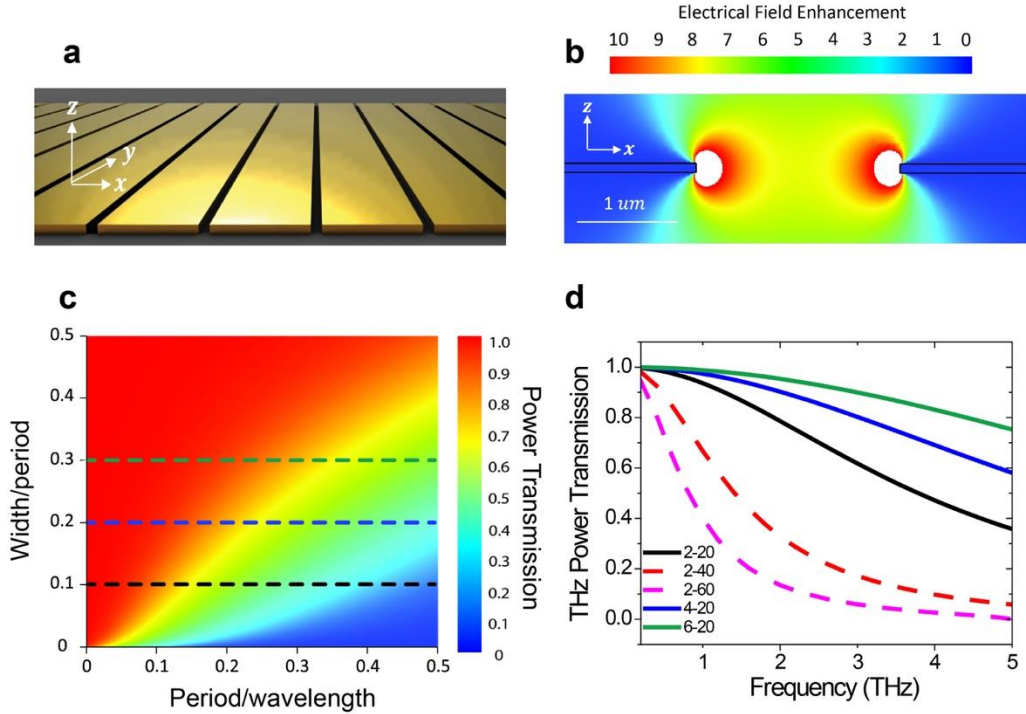


Figure 2-1: Broadband Terahertz metamaterial of periodic gold slits.

(a) Schematic drawing of periodic gold slits suspended in air. (b) Simulated spatial distribution of electrical field enhancement of THz wave for a gold slit of width 2 μm and period 20 μm . The THz wave is polarized along x (perpendicular to the slit). (c) Color plot of power transmission as a function of period to wavelength ratio and slit width to period ratio. (d) Frequency dependent transmission for various geometries. The three solid lines correspond to the dashed line cuts in (c) and show large transmission over a broad range of frequency (black trace is for slit width 2 μm and period 20 μm). Slits with width 2 μm and period 40 μm (red dashed trace) and 60 μm (magenta dashed trace) show decrease of transmission at high frequency. All simulations are performed for gold slit devices which are 80 nm thick and suspended in air.

We perform Fourier Transform (FT) with respect to variable x in both sides of Eq. (2-1). Note that both sides are periodic functions with a period of P . The FT of Left Hand Side (LHS) results in a sum of planar waves for arbitrary z :

$$E_x^{III}(x, z) = \frac{2\pi}{P} \sum_{n=-\infty}^{\infty} \tilde{E}_x^{III}(k_n) e^{i\zeta_n z} e^{ik_n x} \quad (2-2)$$

with $k_n = 2\pi \frac{n}{P}$. The wave vector in z for each term is determined by Helmholtz equation as

$\zeta_n = \sqrt{\left(\frac{2\pi}{\lambda}\right)^2 - k_n^2}$, where λ is the effective wavelength in region III. Eq. (2-2) is also known as

the Rayleigh-Bloch Expansion.

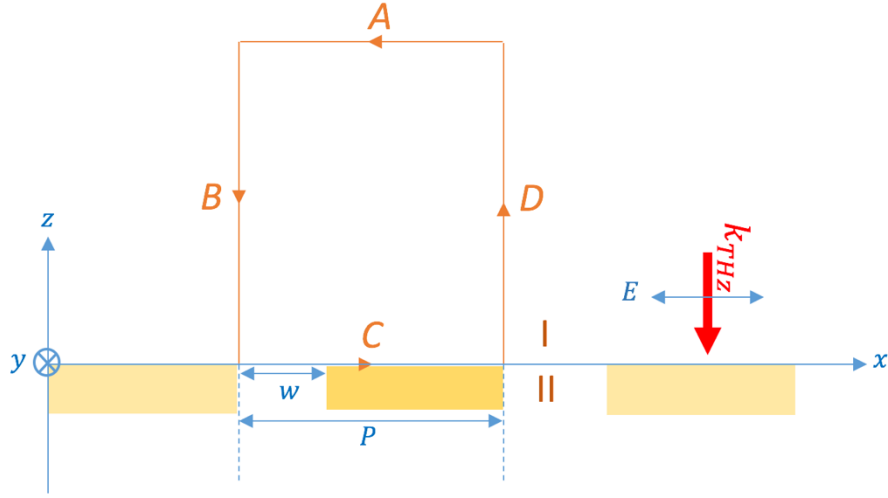


Figure 2-2: Schematic representation of a Faraday Loop (A-B-C-D).

The side C sits exactly at the interface between region I (the side of the incident light) and II (slits array)

In the subwavelength regime (in which the slit-array device is designed to work) where $\lambda > P$, it is easy to see that ζ_n is always imaginary except for the term $n = 0$. Since imaginary ζ_n leads to evanescent waves that decay in z direction and cannot propagate into far field in region III ($z \gg \lambda$), the far field transmission (P_{trans}) is solely determined by the $n = 0$ term of Eq. (2-2). In other words, only the zeroth order of transmission contributes to our measured transmission in experiment.

In the far field limit, we have:

$$E_x^{III}(x, z \rightarrow \infty) = \frac{2\pi}{P} \tilde{E}_x^{III}(0) e^{i\zeta_0 z} \quad (2-3)$$

Therefore, the transmission intensity can be written as $P_{trans} = \frac{1}{2} E_x H_y^* = \frac{|\frac{2\pi}{P} \tilde{E}_x^{III}(0)|^2}{2Z_{III}}$, where Z_{III} is the electromagnetic impedance in region III.

The FT of right hand side (RHS) of Eq. (2-1) can be written in a similar form as well:

$$E_x^{II}(x, z = 0) = \frac{2\pi}{P} \sum_{n=-\infty}^{\infty} \tilde{E}_x^{II}(k_n) e^{ik_n x} \quad (2-4)$$

Substitute Eq. (2-4), (2-2) to Eq. (2-1), we have:

$$\sum_{n=-\infty}^{\infty} \tilde{E}_x^{III}(k_n) e^{ik_n x} = \sum_{n=-\infty}^{\infty} \tilde{E}_x^{II}(k_n) e^{ik_n x} \quad (2-5)$$

By Eq. (2-3), (2-5) and orthogonality of each Fourier Transform component, we can rewrite electrical field at far field in Region III as:

$$E_x^{III}(x, z \rightarrow \infty) = \frac{2\pi}{P} \tilde{E}_x^{III}(0) = \frac{2\pi}{P} \tilde{E}_x^{II}(0) \quad (2-6)$$

On the other hand:

$$\frac{2\pi}{P} \tilde{E}_x^{II}(0) = \frac{1}{P} \int_{-\frac{D}{2}}^{\frac{D}{2}} E_x^{II}(x, z = 0) dx \quad (2-7)$$

Since the tangential field $E_x^{II}(x, z = 0)$ must be zero everywhere on top of gold (gold is assumed to be a Perfect Electric Conductor (PEC) in the THz regime), we have:

$$E_x^{III}(x, z \rightarrow \infty) = \frac{1}{P} \int_{-\frac{w}{2}}^{\frac{w}{2}} E_x^{II}(x, z = 0) dx = \frac{\eta E_0 w}{P} \quad (2-8)$$

where $\eta \equiv \frac{1}{w} \frac{\int_{-\frac{w}{2}}^{\frac{w}{2}} E_x^{II}(x, z=0) dx}{E_0}$ is explicitly the average field enhancement, defined as $\langle \frac{E_{gap}}{E_0} \rangle$, inside the slit. E_0 is the field amplitude of the incident THz wave.

Putting all these pieces together, we have the final expression for THz power transmittance:

$$T = \frac{P_{trans}}{P_{incident}} = \frac{\frac{1}{2Z_I} \left(\frac{\eta E_0 w}{P} \right)^2}{\frac{1}{2Z_{III}} E_0^2} = \frac{Z_{III}}{Z_I} \left(\frac{\eta w}{P} \right)^2 \quad (2-9)$$

where Z_{III} is the impedance of the region for incident light (region III). When the configuration is symmetric, i.e. $Z_I = Z_{III}$:

$$T = \left(\frac{\eta w}{P} \right)^2 \quad (2-10)$$

2.3.2 Local Field Enhancement

In the limit of large period $P/\lambda \rightarrow \infty$, our slit array effectively becomes a single-slit, in which the average field enhancement inside the slit can be calculated exactly using the “local capacitor” λ – zone model⁴⁰. In this model, local field enhancement in the slit originates from opposite charge oscillation (thus accumulation) at both edges of the slit due to surface currents excited by the incident light. The effective “size” of accumulated charge extends to roughly $\sim \lambda$ on both sides of the slit. The amount of charge accumulation within this extension is given by:

$$Q = \frac{\epsilon_0 \lambda}{i\pi} \quad (2-11)$$

The field enhancement in the slit is estimated to be proportional to Q and inversely proportional to slit width w . We have:

$$\eta = \frac{\epsilon_0 \lambda}{\pi w C} \sim \frac{\lambda}{w C} \quad (2 - 12)$$

where C is the effective capacitance of a single slit.

For a small enough wavelength with $P \gg \lambda$, the λ -zone for individual slit is not disturbed by adjacent slits, and Eq. (2-12) is still valid. One immediate conclusion from Eq. (2-12) is that for sufficiently high frequencies ($\lambda \rightarrow 0$), $\eta \rightarrow 0$, hence $T \rightarrow 0$. In general, T decreases with increasing frequency, which agrees with our simulation result.

On the other hand, in the long wavelength limit when $P \ll \lambda$, we can construct a quasi-static Faraday Loop⁴¹ depicted in Fig. 2-2.

Note $E_x^A(x) \approx E_0$ for large enough $|l_B|$ and $E_z^B(z) = E_z^D(z)$ because of the periodic condition.

Also by definition of the average local field enhancement, $\int_C E_x^C dx = \eta w E_0$. Following the Faraday's loop A-B-C-D in the quasi-static limit, we therefore deduce:

$$\oint_{A \rightarrow B \rightarrow C \rightarrow D} E \cdot ds = 0 \rightarrow \eta \sim \frac{P}{w} \quad (2 - 13)$$

This reveals a frequency independent η , in the long wavelength regime, consistent with our simulation. According to Eq. (2-10), we can find the frequency independent transmission T . From the simulation results, we know $T \rightarrow 1$ in the $\lambda \gg P$ limit. Combining this with Eq. (2-10), the Eq. (2-13) can be written exactly as $\eta = \frac{P}{w}$, which is also the maximum value for field enhancement in the slit according to Eq. (2-10). This maximum enhancement is therefore solely determined by the geometry and can be improved through miniaturization of the slit w for any a fixed period P . It

can be, in principle, extremely high up to a limit imposed by the state of the art technology of lithography.

Eq. (2-12) and Eq. (2-13) reveal distinctively different behavior of η . In the short wavelength regime, η diminishes for shorter wavelengths while it remains a constant upon long wavelength excitation. The power transmittance T changes accordingly. A “cross-over” point can be defined between these two regimes where $T = 0.5$.

A rigorous solution for η for entire range of λ including the “cross-over” can be found in Ref⁴¹ from an electron-dynamic point of view, or using general wave expansion techniques like the Rigorous Coupling Wave Analysis (RCWA)²³.

By Eq. (2-8), we know the far field transmission T is directly related to the average local fields inside each slit. We therefore expect a large modulation of the THz wave transmission if we couple the periodic slits with an active load which can modify the local field significantly. As mentioned before, graphene is an ideal candidate for this active load because of its highly tunable conductivity at THz^{42,43}. When gated sufficiently, the conductivity of graphene can be increased by more than 10 times from its minimum conductivity⁴⁴ at CNP ($\sim 4 G_0$). At the same time, graphene has a non-resonant Drude response to THz wave, which is essential to operate the hybrid modulator over broad frequency range. Moreover, being atomically thin, graphene is flexible can be strongly coupled to the enhanced near field in the slit.

2.4 EXPERIMENT

We fabricate a novel hybrid device by coupling a single layer graphene sheet to a broadband THz metamaterial and achieve extraordinary THz wave power modulation by controlling the graphene conductivity through electrostatic gating. This THz metamaterial, made of periodic gold slit array, shows close to unity THz transmission over broad range of frequency that arises from the coherent radiation of greatly enhanced near field in the slits. Graphene coupled to this metamaterial acts as an active load which significantly modifies the near field when doped efficiently. We also show that this strong coupling between graphene and the metamaterial device gives rise to a large enhancement of absorption of graphene even when the graphene is charge neutral. This hybrid graphene-metamaterial device therefore provides a new platform for future nonlinear THz investigation of graphene. The broadband nature of this hybrid device is particularly advantageous for nonlinear THz spectroscopy study considering the limited intense THz sources available.

2.4.1 Device Fabrication

To describe our experiment in detail, we first transfer a single layer graphene grown by chemical vapor deposition method (CVD)⁴⁵ to a 2-20 μm gold slit device on 300 nm SiO₂/ Si substrate. We define the source, drain and gate electrodes on graphene using a shadow mask and gate graphene electrostatically using ion-gel⁴⁶, as schematically shown in Fig. 2-4a. During the THz transmission measurement, we vary the gate voltage to control the density of carriers in graphene and simultaneously monitor the resistance of the device by applying a small bias across the source-drain electrodes. This simultaneous electrical transport measurement helps to determine the charge neutral point (CNP) of graphene (~ 0.33 V in Fig. 2-4c). Fig. 2-4b shows that when the graphene is charge neutral the transmitted THz wave through the hybrid device (blue trace) shows a small phase shift compared with the transmitted THz wave through the reference sample of SiO₂/Si chip,

while the most obvious change is the decrease of the peak value near sampling delay $\tau = 0$ ps. Since the THz transmission spectrum of the device is relatively flat in the frequency window of our THz source, we can use the change of the peak value to estimate the transmission of the hybrid device, which is roughly $\sim 84\%$ when the graphene is at CNP and $\sim 43\%$ for graphene gated at -2 V away from the CNP.

2.4.2 Conductivity of graphene sheet in the slit

To verify our theory of THz modulation, it is necessary to determine the actual conductivity of graphene sheets within slit gaps during experiment. For the devices in Fig. 2-4a, we simultaneously measure the resistance of the device in a two terminal geometry by applying a small bias. The resistance we measure is the sum of contact resistance and that of graphene sheet carrying current. Considering the geometry factor and assuming a gating capacitance for ion gel, we have the following expression:

$$\begin{aligned}
 R &= R_{contact} + \frac{1}{ge\mu \sqrt{n_{imp}^2 + \left(\frac{C|V - V_{cnp}|}{e}\right)^2}} \\
 &= R_{contact} + \frac{1}{ge \sqrt{(\mu n_{imp})^2 + \left(\frac{\mu C|V - V_{cnp}|}{e}\right)^2}}
 \end{aligned} \tag{2-14}$$

Where V_{cnp} is the charge neutral point (CNP) of graphene, C is the gating capacitance, V is the gating voltage for electrostatic gating, μ is graphene mobility, n_{imp} is impurity doping at $V = V_{cnp}$, g is geometry factor of the graphene piece in study, and e is the electron charge.

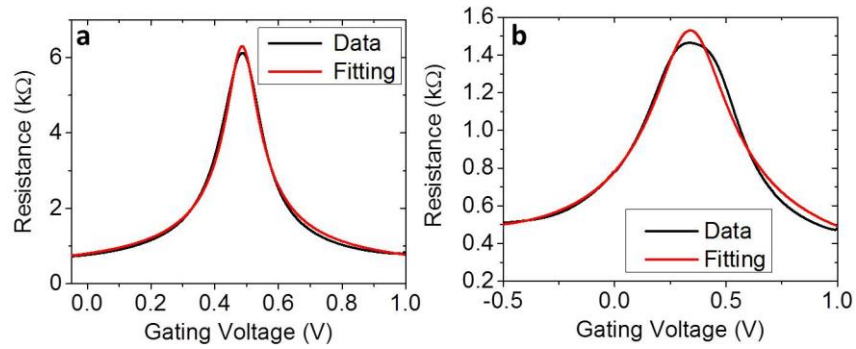


Figure 2-3: Electrical transport characterization and the THz transmission modulation.

- (a) Resistance measured for the bare graphene device on SiO₂/Si substrate. (b) Resistance measured for the graphene-slit array hybrid device on SiO₂/Si substrate.

For our control device of bare graphene, we measure the geometry ratio to be $g = \frac{w}{L} = \frac{2}{3}$. For the slit hybrid device where the major conducting channel is the graphene outside of slit array (graphene on top of gold slit array is shorted), we measure the geometry ratio to be $g = \frac{w}{L_{out}} = 4$.

For both devices, we fit the experimental data according to Eq. (2-14). We fix the values for $g, V_{cnp} \cdot R_{contact}, \mu n_{imp}$ and μC are fitting parameters. V is the fitting variable.

For the control device, $R_{contact} = 191.6 \pm 9\Omega$, $\mu C = (5000 \pm 40)\mu F/(Vs)$, $\mu n_{imp} = (1537 \pm 7) \times 10^{12}/(Vs)$. The value of μC agrees with previous studies for ion-gel gated graphene^{13,47}, where $\mu \sim 1000 cm^2/(Vs)$ and $C \sim 6\mu F/cm^2$. For the graphene-slit hybrid device, we have the best fitting (red trace in Fig. S3b) with the fitting parameters $R_{contact} = 140 \pm 5\Omega$, $\mu C = (1124 \pm 8)\mu F/(Vs)$, $\mu n_{imp} = (1156 \pm 4) \times 10^{12}/(Vs)$.

With the value of $R_{contact}$, we can extract graphene sheet conductivity for different gate voltages using:

$$\sigma = \frac{1}{(R - R_{contact})g} \quad (2 - 15)$$

We use this derived graphene sheet conductivity to plot Fig. 2-5c.

2.4.3 Measuring THz transmission

By monitoring the peak value change, we obtain the normalized transmission change as a function of gate voltage as shown in Fig. 2-4d.

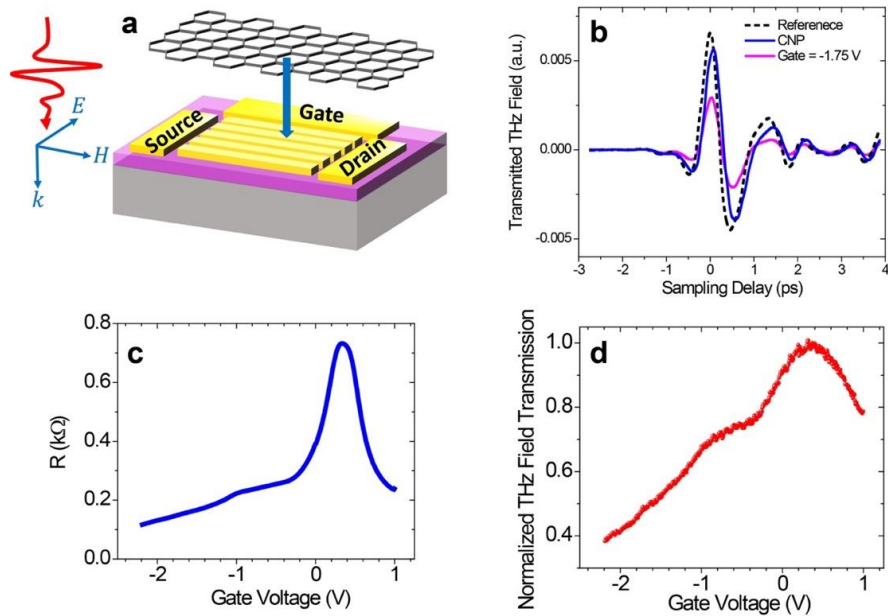


Figure 2-4: THz modulation by the graphene/metamaterial hybrid device.

(a) Schematic representation of the experiment setup for measurement as well as the hybrid device configuration. We fabricate the hybrid device by transferring a single layer graphene on top of a gold slit device of width $2\ \mu\text{m}$ and period $20\ \mu\text{m}$. The incoming THz wave is polarized perpendicular to the slit orientation. (b) Transmitted THz waveforms for a reference sample (dashed black trace), the hybrid device with graphene at CNP (solid blue trace), and the hybrid device with graphene at gate voltage $-1.75\ \text{V}$ (solid magenta trace). (c) Resistance measured for this hybrid device shows CNP at the gate voltage of $0.33\ \text{V}$. (d) Simultaneously measured THz field transmission of this hybrid device (normalized to the transmission when graphene is at CNP).

This change of transmission through the hybrid device (red dots in Fig. 2-4d) closely correlates to the graphene conductance we measure simultaneously (Fig. 2-4c): the transmission being the highest when the graphene is charge neutral and the lowest when the graphene conductance is the highest. The field modulation, defined as $\frac{|E_{\text{max}}| - |E_{\text{maxmin}}|}{|E_{\text{max}}|}$, is as large as $\sim 60\%$ when the gate

voltage is at -2 V. This field modulation corresponds to a power modulation (defined as $\frac{P_{max}-P_{min}}{P_{max}}$) of $\sim 82\%$, which is about 4 times larger than previous result using bare graphene.

Fig. 2-5 shows a summary of our device together with its transmission modulation as we gate the graphene. In an FEM simulation shown in Fig. 2-5b, it is clear that the local field enhancement changes with graphene conductivity accordingly, supporting our underlying claims. In Fig. 2-5c, we explore the modulation performance of a miniaturized device ($0.1\text{-}2\ \mu\text{m}$), projecting it to be as high as 95%.

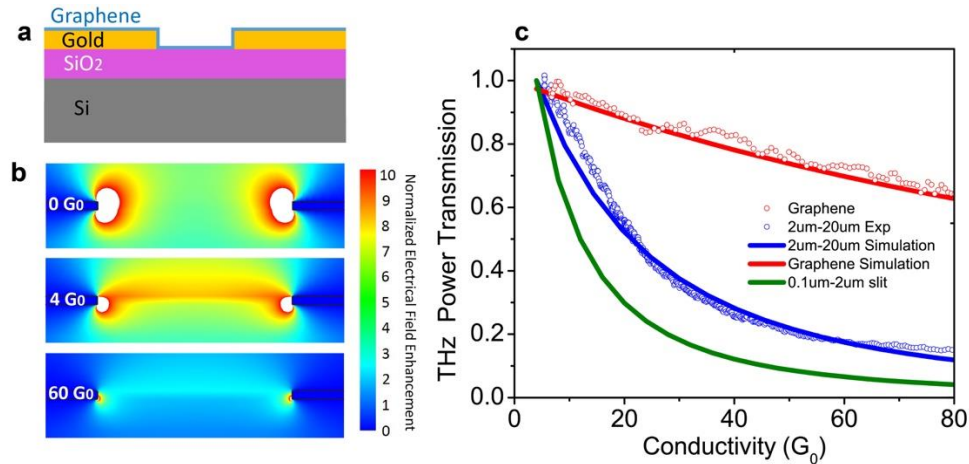


Figure 2-5: THz modulation depth vs. graphene conductivity.

(a) Schematic drawing of the side view of the hybrid device. (b) Simulated field enhancement factor in the slit for the hybrid device when there is no graphene ($0\ G_0$), graphene conductivity at $4\ G_0$, and graphene conductivity at $60\ G_0$, respectively. The slit device is of width $2\ \mu\text{m}$ and period $20\ \mu\text{m}$. (c) Normalized THz power transmission modulation as a function of graphene conductivity. The solid line traces are simulation results for bare graphene (red) and the hybrid device (blue). The empty dots are experimental data for bare graphene (red) and the hybrid device (blue), and we fit the experimental data to the simulation result with the contact resistance being the only fitting parameter.

2.5 CONCLUSION

In summary, we systematically investigate, both in theory and in experiment, a broadband THz metamaterial of periodic gold slits that exhibits near unity transmission over a broad range of frequencies. We attribute the large THz transmission to the coherent radiation from the enhanced near field in the slits, and this transmission can be greatly modulated by modifying the near field enhancement. We achieve so in a proof of concept demonstration by coupling a single layer CVD graphene to the metamaterial device and controlling the conductivity of graphene through electrostatic gating. Our broadband hybrid device shows much larger THz modulation than a bare graphene device, which itself is much improved compared to the previous semiconductor modulator. We also show the possibility for further improvement through miniaturization of the slits. At last, this hybrid device provides a new platform to realize strong light matter interaction in graphene, providing a design framework to future nonlinear THz studies.

3 TUNABLE DARK MODES IN ONE-DIMENSIONAL “DIATOMIC” DIELECTRIC GRATINGS

3.1 MOTIVATION

Planar optical resonators with high quality factor (Q) modes are important in modern photonic technologies. Their applications range from sensing⁴⁸⁻⁵⁰, filtering⁵¹⁻⁵⁴, display⁵⁵⁻⁵⁷ to laser and optical interconnects^{58,59}. The planar design has attracted much attention in research because of its benefits of easy fabrication and potential compatibility for on-chip integration with other optoelectronic components⁶⁰⁻⁶². Compared to the small mode-volume and defect-based counterparts⁶³⁻⁶⁶, delocalized modes, most notably the guided waves in photonic crystal slabs, allow free space excitation and better coupling efficiency with quantum well or 2D materials like graphene or transition metal dichalcogenides^{61,67,68}. Ultra high Q resonances in photonic crystal slabs have been proposed and demonstrated in various designs, a recent example being the high contrast gratings (HCG)^{54,69,70}. However, their optimization towards robustness and tunability is generally lacking.

Therefore, we are motivated to study a new class of subwavelength 1D dielectric gratings with two nonequivalent subcells in each period, referred to as “diatomic” gratings. These “diatomic” gratings have great design flexibility as they support structurally defined “dark modes”. Q factors of these “dark modes” are robust against strong external perturbation and their resonance can be tuned continuously, for instance, by mechanically stretching the grating in-situ. When suspended in air, our optimized “diatomic” design boasts a much thinner geometry, higher Q and better in-situ tunability compared to conventional HCGs^{71,72}. At resonance, electrical fields of the “diatomic” grating are largely concentrated in its air gap, making it a suitable device for sensing. The

“diatomic” grating acts effectively as a thin layer of low refractive index medium with tunable resonances and exposed fields, making it a potentially useful platform to various applications.

3.2 THEORY

3.2.1 Dark modes in grating

A “dark” mode is an electromagnetic eigenmode of an optical system that has very small radiative coupling (κ) to far fields^{73,74}. The concept of “dark” mode is central to many novel optical phenomena including Fano resonance (FR) and electromagnetically induced transparency (EIT)^{75–77}. For an optical cavity, κ is usually related to $1 - |r|^2$, where r is the complex mode reflectivity at the cavity interfaces (e.g. $z = 0$ or $z = t$ in Fig. 3-1a). Compared with “bright” modes, photons in a “dark” mode experience longer lifetime in the cavity and thus higher Q because of the effectively larger r . This leads to ultra-high Q resonances in dielectric structures where other types of photonic energy loss are negligible.

For a guided mode in subwavelength gratings, κ is qualitatively determined by the field overlap between this mode and the zeroth order reflection or transmission plane wave at the interfaces $z = 0, t$ respectively^{78,79}. In particular, with normal incidence and TM polarization which is our main focus in this paper, κ can be written as:

$$1 - |r|^2 \equiv \kappa \propto \frac{\left| \int_0^P E_x dx \right|_{z=0,t}^2}{P} \quad (3 - 1)$$

where P is the period of the grating and E_x is the x component of the electrical field of the mode at the interface $z = 0$ or $z = t$. r and κ are the same for both reflection ($z = 0$) and transmission ($z = t$) interfaces when the grating is suspended in air.

The reduced Brillouin zone and coupling behavior of a regular subwavelength 1D grating (schematic view in Fig. 3-1a) is illustrated in Fig. 3-1b. With normal incidence, only modes at the zone center (Γ point) can be excited in the grating, if scattering from grating edges are to be ignored. Due to the overall reflection symmetry of the 1D grating, both even and odd modes are present at the zone center. The even modes are “bright” modes that couple strongly to the far-field radiation (red dots in Fig. 3-1b), and the odd modes are completely “dark” with zero coupling (dark dots)⁸⁰. The modes at finite κ , in particular those close to the zone edge, cannot couple to the normal incident because of large momentum mismatch. Those modes (gray dots) are otherwise considered “dark” because $\kappa \approx 0$ owing to the field’s sign change in one unit cell ($k_x \rightarrow \pi/P$).

3.2.2 Zone folding

The zone edge “dark” modes can be folded back to Γ point by breaking the symmetry of adjacent unit cells in the grating, after which they gain a small but finite κ to the normal incidence. In this process, which is also known as “zone folding”, two adjacent unit cells (referred here as subcell 1 and subcell 2) merge into a bigger one, illustrated in Fig. 3-1c. We call such 1D gratings with two subcells in one period “diatomic” gratings. It is worth noting that a similar symmetry breaking concept, called the “doubly periodic grating”, has been previously proposed to improve the angular tolerance of guided mode resonances^{81–85}. However, the Q of these resonators remain relatively low ($\sim 8,000$) and their dark mode aspects are largely unexplored.

One can engineer the asymmetry between the subcells to control the behavior of the grating with great flexibility. Here we focus on the cases that the two subcells are identical except for their air gaps. This asymmetry is captured by $\delta = \frac{|a_1 - a_2|}{P}$, where a_1 and a_2 are the widths of the corresponding air gaps and P is the grating period. $\gamma = \frac{2s}{P}$ is the dielectric filling factor and s is

the width for each dielectric bar in the subcells (Fig. 3-1c). In our case, the dielectric bar is made of silicon ($n_{dielectric} = 3.48$). When $\delta = 0$, the design is identical to a regular grating. However, when $\delta \neq 0$, the zone edge “dark” modes are folded back to Γ point in the Brillouin Zone with finite κ , shown as the gray dots in Fig. 3-1d.

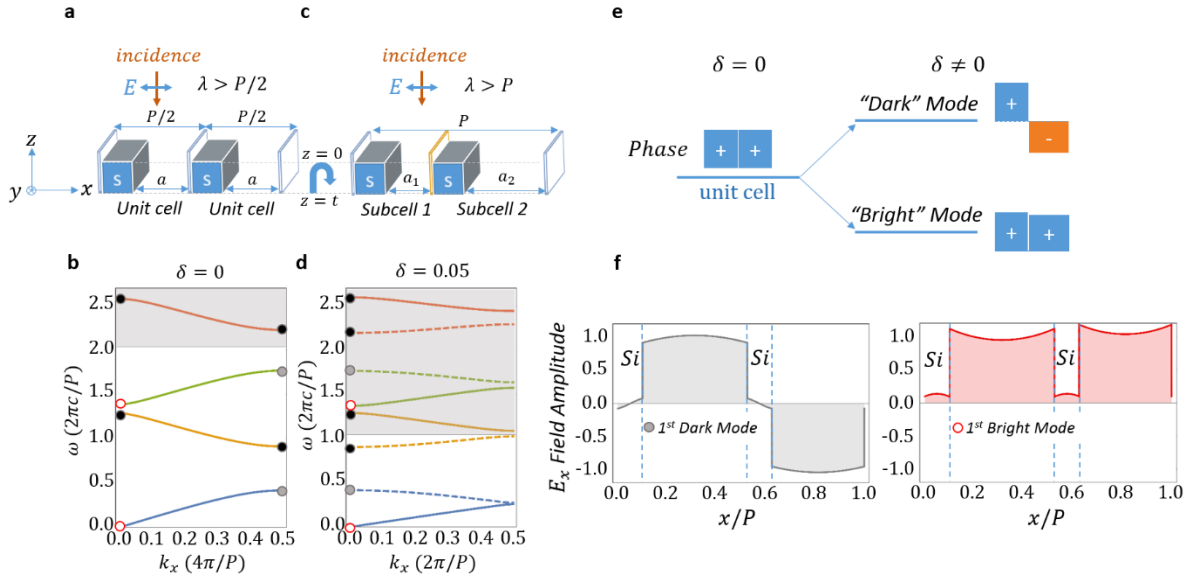


Figure 3-1: Design of the Double Bump and the emergence of intrinsic “dark” modes.

a) Schematic diagram of the regular grating. Excitation is with normal incidence and TM polarization. Grating parameters: thickness t , period $P/2$ and filling factor γ . Grating incidence and transmission interfaces are at $z=0$ and $z=t$, respectively. b) Brillouin zone of a typical regular grating. Red dots represent “bright” modes at the zone center and dark dots represent completely “dark” modes due to particular symmetries in the grating. Gray dots represent “dark” modes with a small but finite κ at the zone edge. c) Schematic diagram of a double bump grating with the same filling factor γ , thickness t except for a doubled period P and finite air gap difference δ . Two subcells merge into a larger unit cell. d) Brillouin zone of a typical double bump grating with $\delta=0.05$. e) Illustration of emergence of a pair of odd/even modes from the “bright” eigenmode in terms of symmetry breaking. f) The field profile for E_x for the 1st order “bright” and “dark” eigenmodes in the double bump design.

It is important to note that the 1st order “dark” mode (the gray dot in the dashed blue curve of Fig. 3-1d) is guaranteed to exist in the subwavelength regime as long as $\gamma \neq 0$ and $n_{dielectric} > 1$, even at large incidence angles when $k_x \gg 0$. This is easily checked as the result of gap opening due to the non-uniform $\epsilon(x)$ in the grating. The dispersion of the fundamental mode (blue curve) in Fig.

3-1b always bends downwards from the light cone, ensuring $\omega_{1st\ dark\ mode} < \frac{2\pi c}{P}$. The emergence of these “dark” modes in the zone center can also be viewed as mode splitting in Fig. 3-1e, where a pair of even and odd modes are created from the originally “bright” mode after symmetry breaking. The odd mode has weak coupling to far field radiation due to the destructive interferences from its two subcells, corresponding to a “dark” mode. Typical electrical field profiles for the 1st order “bright” and “dark” modes of the “diatomic” grating ($\delta = 0.05, \gamma = 0.2$) are shown in Fig. 3-1f. The mode profiles and band structures in the Brillouin zone are calculated using numerical methods described in Ref²².

3.2.3 Diatomic structures

The “diatomic” structure is completely defined with three parameters: grating period (P), dielectric filling factor (γ) and the subcell difference (δ). When $\delta \neq 0$ but $\delta \ll 1$ (that is, $|a_1 - a_2| \rightarrow 0$), it is straightforward to estimate the coupling coefficient κ for the “dark” modes represented in Fig. 3-1e:

$$\kappa \propto \frac{\left| \int_0^P E_x dx \right|^2}{P} = \frac{\left| \int_0^{s+a_1} E_x dx - \int_{s+a_1}^P E_x dx \right|^2}{P} \propto \delta^2 \rightarrow 0 \quad (3-2)$$

Eq. (3-2) follows because for small δ , the mode profile in subcell 1 and subcell 2 are approximately the same except for a sign change. The “diatomic” design not only makes those “dark” modes accessible to zone center excitation, but more importantly, it can engineer their “darkness” (κ) by proper choice of δ . In addition, Eq. (3-2) depends solely on the design (P, γ, δ) itself. As a result, the Q and the existence of these “dark” modes are expected to be robust even under strong external perturbation.

3.3 SIMULATION

3.3.1 Q factor of dark mode resonance

Fig. 3-2b shows the simulated reflection spectrum for various filling factors γ in a thin “diatomic” grating using rigorous coupled-wave analysis (RCWA)¹⁶. The grating design parameters are $\delta = 0.05$ and $\frac{t}{P} = 0.1$. Focusing on the sharp resonance of the “dark” mode, we see marked decline in Q (Fig. 3-2a) from 10^8 to 10^5 with γ varying from 0.1 to 0.5. The resonance wavelength λ_{res} is slightly red-shifted due to a larger n_{eff} . The fall in Q can be qualitatively understood by an increased mixing between “dark” and “bright” modes in the grating, leading to reduced effective $|r|$ for the “dark” mode. Intuitively, an increase in γ (thus n_{eff}) helps to excite more “bright” modes in the grating and as a result, photonic loss rises in general because of their contribution of stronger coupling to the far fields.

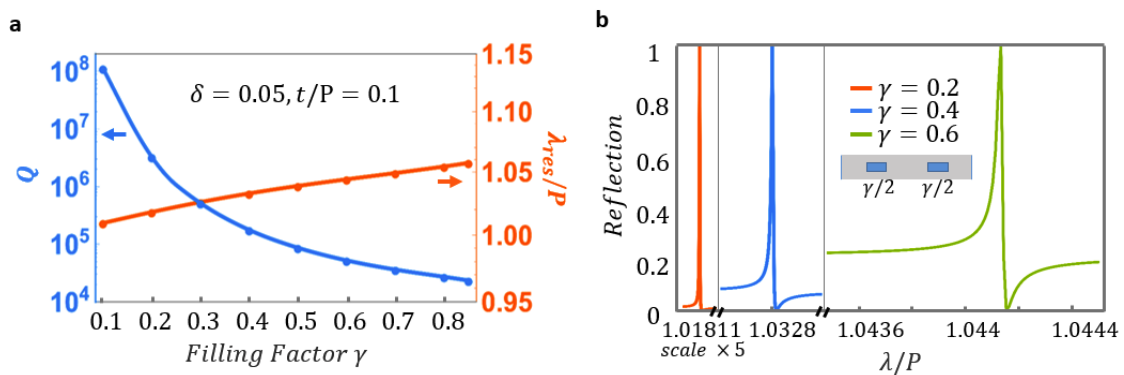


Figure 3-2: Dependence of Q on filling factors for the “diatomic” design

(a) Dramatic decline in Q for the dark mode resonance as a result of increased filling factor and subsequent increased mixing with “bright” modes. (b) Reflection spectrum showing resonances of varying Q for 3 different filling factors. Inset shows a unit cell of the “diatomic” grating with given design parameters.

For design parameters $\delta = 0.05$ and $\frac{t}{p} = 0.5$, we see in Fig. 3-3a that indeed more “bright” mode resonances are present with larger γ , producing complex beating patterns as an unfavorable spectroscopic background. The presence of “bright” modes is more pronounced in a thick grating compared to thinner ones. In Fig. 3-3a, each of the sharper resonances corresponds to a “dark” mode, while λ_{res} is determined with round trip condition $\phi_{round} = 2\pi n$ (color line in Fig. 3-3c).

3.3.2 Interaction between bright and dark eigenmodes

A closer look at Fig. 3-3b reveals that the reflectivity $|r|$ at the corresponding first order resonances λ_{res} ($\phi_{round} = 2\pi$, color markers in Fig. 3-3c) falls as γ is increased. One can also verify that with larger γ , more “bright” modes (gray lines in Fig. 3-3c and Fig. 3-3b) with much smaller $|r|$ start to resonate. The exact behavior of mixing between “dark” and “bright” modes is complicated but it explains well the declining trend of Q factors seen in Fig. 3-3a. We conclude that Q degrades with γ . Our observation also reflects the difficulty to achieve high Q resonances in a beat free background in other grating designs like the HCG, as they generally rely on a complicated mixing of “bright” modes that requires large grating thicknesses⁷⁰.

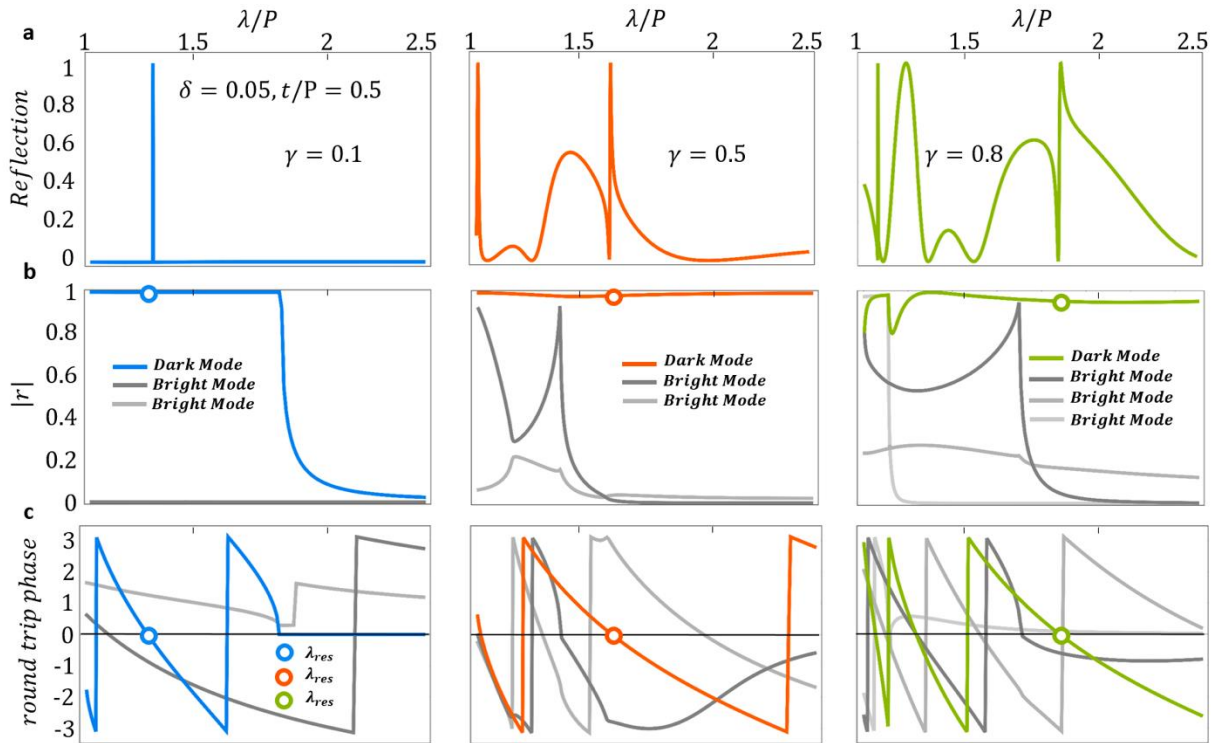


Figure 3-3: Demonstration of the effect of filling factors on the double bump design.

a) Emergence of beating from additional bright mode resonances for large filling factor γ in a thicker grating design. b) Decline in $|r|$ for the “dark” supermode (color line) due to mixing with bright modes. c) Round trip phase for various modes. The “dark” mode is plotted in color. It predicts well where the sharp resonance is and shows the emergence of new resonances from “bright” modes as γ increases.

We then study the Q dependence on γ more carefully with an example of a thicker “diatomic” grating. For design parameters $\delta = 0.05$ and $t/P = 0.5$, we see in Fig. 3-3a that indeed more “bright” mode resonances are present with larger γ , producing complex beating patterns as an unfavorable spectroscopic background. The presence of “bright” modes is more pronounced in a thick grating compared to thinner ones. In Fig. 3-3a, each of the sharper resonances corresponds to a “dark” mode, while λ_{res} is determined with round trip condition $\phi_{round} = 2\pi n$ (color line in Fig. 3-3c). A closer look at Fig. 3-3b reveals that the reflectivity $|r|$ at the corresponding first order λ_{res} falls as γ increases. One can also verify that with larger γ , more “bright” modes (gray lines in Fig. 3-3c and Fig. 3-3b) with much smaller $|r|$ start to resonate. The exact behavior of mixing

between “dark” and “bright” modes is complicated but it explains well the declining trend of quality factors seen in Fig. 3-3a. We conclude that Q degrades with γ . Our observation also reflects the difficulty to achieve high Q resonances in a beat free background in other grating designs like the HCG, as they generally rely on a complicated mixing of “bright” modes that requires large grating thicknesses⁷⁰.

3.3.3 A representative design

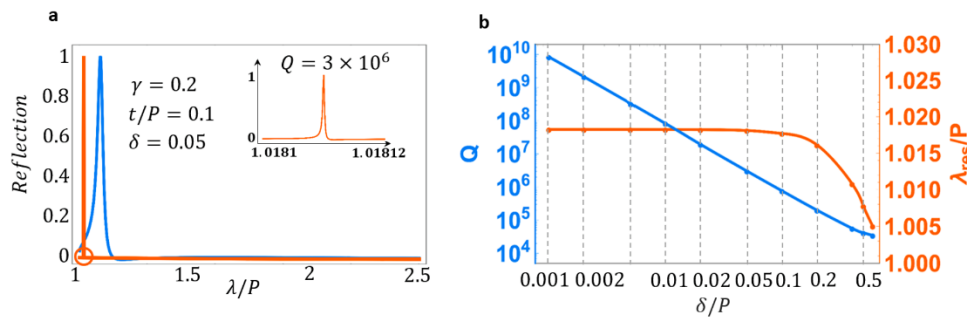


Figure 3-4: The design of a typical single high Q resonance in “diatomic” grating.

(a) The single high Q resonance in the “diatomic” grating (red) and the corresponding regular grating (blue). (b) Power law dependence of Q (blue) as a function of δ/P for the “dark” mode resonance. The resonance wavelength barely changes during the tuning (red).

In Fig. 3-4a, we show a characteristic single high Q ($\sim 10^6$) resonance under TM and normal incidence (red curve) for the “diatomic” grating. The design parameters are $\gamma = 0.2$, $\delta = 0.05$ and $t/P = 0.1$, where the dielectric filling is silicon ($n = 3.48$) and the grating is suspended in air. It is much thinner and has a much smaller dielectric filling factor compared to other high Q gratings like the HCG^{70,78}. The $\omega - \beta$ dispersion plot²² is calculated and it shows the 1st order “dark” and “bright” modes (blue dashed and solid lines, respectively) excited in the grating in the subwavelength regime, while β is the propagation constant in z for a given frequency ω . The 2nd order “dark” mode (orange dashed line) is not excited because it is “completely dark” due to the

reflection symmetry in the grating⁸⁰. For thin “diatomic” gratings, the “dark” mode gives rise to a single sharp resonance in the spectrum, free of off-resonance contributions.

We note that its resonance wavelength is very close to P ($\frac{\lambda_{res}}{P} \approx 1.018$) and this makes the grating an optically thin ($n_{eff}t/\lambda_{res} \approx (\gamma(n-1) + 1)t/\lambda_{res} \approx 0.15$) design. A zoom-in of the resonance is shown at the inset of Fig. 3-4a. The slight Fano shape indicates a weak interaction between the “dark” and the “bright” modes⁸⁶. Compared to the Q factor (~ 40) of the guided mode resonance of a regular but otherwise identical ($\delta \approx 0$) grating, Q in the “diatomic” grating is increased by more than 20,000 times (blue curve in Fig. 3-4a). This impressive Q is achieved with a subcell difference $\delta = 0.05$, 5% of the period length P . A more aggressive design of $\delta = 0.02$ will push the Q up to 10^7 as shown in Fig. 3-4b and this is possible (for example, when $0.5\mu m < P < 1\mu m$) using the state of the art fabrication techniques. Similar performance is observed when the “diatomic” grating sits on a substrate.

In the log-log plot of Fig. 3-4b, Q diverges as $\delta \rightarrow 0$. When $\delta = 0$ exactly, the “dark” mode resonance disappears due to its complete darkness. The scaling law of Q on δ is consistent with Eq. (3-2). It is notable that the resonance wavelength λ_{res} remains flat for a broad range of δ up to $\delta = 0.1$, indicating that while $|r|$ of the “dark” mode varies dramatically, its round trip phase is not much affected by δ with changes by as large as 100 times. Therefore the parameter δ provides an effective control of Q in the design of “diatomic” gratings. From Eq. (3-2), one can obtain the approximate relation for fabrication tolerance of Q in terms of δ as $\frac{d\delta}{\delta} \sim \left| \frac{dQ}{Q} \right|$, a linear relation.

Additionally, we can infer from Fig. 3-4b that the fabrication tolerance for λ_{res} in terms of δ is extremely high. In Fig. 3-4c, we also see that the enhanced (up to 10^5 times) E_x field is largely concentrated in air gaps at resonance, consistent with the field profile for the 1st “dark” mode

plotted in Fig. 3-1d. This is very similar to plasmonic resonators designed for sensing⁸⁷, except that the parasitic photonic loss in metal is absent⁸⁸. This very thin ($\frac{t}{p} < 0.1$) and very small filling factor ($\gamma \leq 0.2$) design makes the “diatomic” grating appealing for sensing applications that require both high Q resonance and a planar geometry for potential integration with 2D materials⁶⁸.

3.3.4 In situ tunable resonator: a possible application

One major advantage of the symmetry-broken “dark” modes in “diatomic” gratings is their robustness to strong external perturbation. This is expected in our previous discussion because of their structurally defined κ . As an important example, resonance wavelength (λ_{res}) of those dark modes can be tuned continuously in-situ without degrading the Q, while the perturbation is provided by stretching the grating using a flexible substrate.

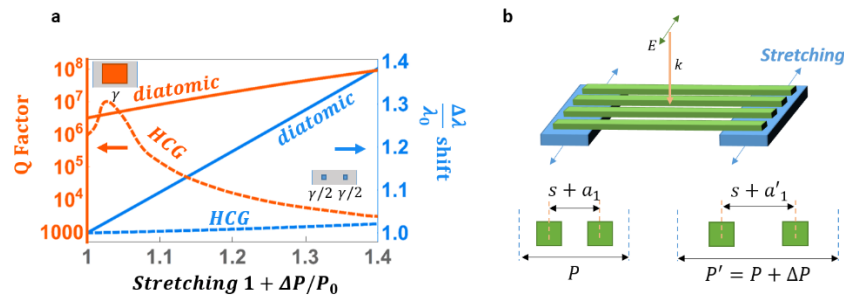


Figure 3-5: In-situ tuning of the high Q resonance in “diatomic” gratings

- (a) Solid and dashed curves represent the simulation results of a typical “di atomic” and HCG grating respectively.
 (b) A schematic view of the structure that allows for in-situ mechanical tuning of the grating period.

A possible way to realize this idea is to embed silicon nano-pillars in the flexible PDMS substrate followed by the subsequent removal of PDMS to create a window of suspended silicon bars. The structure is supported by remaining PDMS at its periphery as illustrated in Fig. 3-5b. By stretching PDMS using electro-mechanically applied stress (MEMS, for example), we can vary the period P

in-situ, while the widths of silicon bars remain unchanged. As a result, phase of the reflectivity of the “dark” mode in the grating is continuously tuned⁷⁹ and λ_{res} is shifted.

We study the tuning capability of the stretched “diatomic” grating by simulating its reflection spectrum using RCWA. The design parameters are $\gamma = 0.2$, $\delta = 0.05$ and $t/P = 0.1$. A tuning range ($\Delta\lambda/\lambda_0$) of 40% achieved by stretching the substrate up to 1.4 times is shown in Fig. 3-5a (blue solid line). The orange solid curve shows a sustained high Q cross the tuning range without deterioration. To compare with a representative regular grating (HCG) that also supports high Q resonances⁷⁰, the improvement of Q in the “diatomic” grating is up to 1000 times and its tuning range is ~ 10 times better. The tuning capability of the “diatomic” grating approaches that of the ideal case with invariant λ_{res}/P . This is desirable for applications that requires optimal tunability, like a tunable pixel in a display⁸⁹. The “diatomic” grating is therefore an appealing candidate for planar resonators with tunable high Q resonances, whose practical design is still lacking to our best knowledge.

3.4 SUMMARY

One major advantage of the symmetry-broken “dark” modes in “diatomic” gratings is their robustness to strong external perturbation. This is characteristic in the “diatomic” grating since: 1, the existence of 1st order dark mode in the subwavelength regime is guaranteed and 2, the κ of the “dark” mode is structurally defined and it is minimally affected during stretch. The tuning capability of the “diatomic” grating approaches that of the ideal case (invariant λ_{res}/P) because $\lambda_{res} \approx P$ always holds in the design. The “diatomic” grating is therefore an appealing candidate for planar resonators with tunable high Q resonances, whose practical design is still lacking to our best knowledge.

To sum it up, we have theoretically studied a new class of 1D subwavelength gratings that supports tunable high Q resonances by breaking the symmetry between its unit cells. Optimization of the new structure, called the “diatomic”, results in an ultra-high Q resonance in a thin grating with small filling factors. It offers unique advantages in terms of design flexibility and high Q sensing. Most importantly, we show that the resonance wavelength of the “diatomic” grating can be tuned in-situ, exhibiting a close to ideal tuning range without compromising its Q. This work provides insight and design guidelines for this new class of planar resonators that are appealing to a wide range of applications including optical sensing, filtering and displays.

4 HIGH Q METALLIC RESONATORS USING DIATOMIC DESIGNS

4.1 MOTIVATION

Plasmonic resonators³³ have been an active research field for its capability of realizing extremely enhanced local fields, a result of strong light confinement thanks to the large refractive index in metal. This local field enhancement is appealing for applications ranging from sensing, nonlinear optics and platforms for strong light-matter interaction^{33,75,90}. By Purcell's effect, local field enhancement can increase by many folds given a larger Q and similar mode volumes, a condition many experiments looking for strong light-matter interaction requires. Additionally, an improved Q can boost sensitivity in plasmonic sensors, making it a key to engineer around in such applications. Traditional plasmonic resonators like split-ring and subwavelength waveguides⁹¹, however, suffer from low Quality factors (Q) generally due to both the intrinsic Joule loss in metal and poor control of free space coupling. Here we present a design that achieves high Q in plasmonic resonators by control of its mode reflectivity using a diatomic grating structure⁹². This special design allows us to model the resonance as Fabry-Perot cavities and tune the equivalent end-mirror reflectivity effectively. Analogous to a Fabry-Perot resonator, free space coupling of plasmonic resonators sets the mode reflectivity at cavity ends, from which Q can be determined. With proper design, critical coupling of the resonator can be realized where Q is much higher than conventional plasmonic devices. The nature of our design is explained in the following theory section where anti-symmetric modes that minimize far field coupling⁷³ play a key role. The theory presents an important view for plasmonic structures as it explores how resonant modes in adjacent cavities interact with each other. Its solution could also lend help to our better understanding of the high Q modes in diatomic gratings.

4.2 THEORY

4.2.1 MDM waveguide

Metal-dielectric-metal (MDM) waveguides are the constituent elements for the metallic cavity grating we study. It is a waveguide where a dielectric is sandwiched between metals. Shown in Fig. 4-1, let the width of the dielectric to be d , and the structure is infinite in the other two dimensions (y and z):

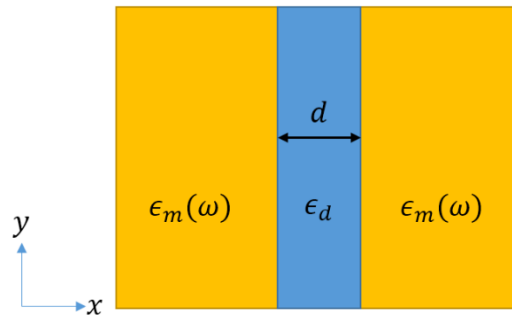


Figure 4-1: A typical MDM configuration with dielectric width d .

Permittivity for the dielectric and metal are represented by $\epsilon_d, \epsilon_m(\omega)$, respectively.

Propagating eigenmodes can be solved analytically from Maxwell's Equations for the MDM layered structure. Specifically, in the subwavelength regime where $d \ll \lambda$, the only propagating mode along y is a fundamental TM mode. It is due to both the extremely small mode width and the strong suppression of electrical fields parallel to metal interface. In such cases, the field distribution of this TM mode resembles much like a TEM plane wave mode and it is concentrated inside the dielectric. Therefore, a subwavelength MDM cavity can achieve impressive mode confinement as well as reduced optical power loss in metal. It is responsible for extraordinary transmission in metal hole arrays as reported in many research articles^{93,94}, and has been useful for plasmonic devices in a broad range of applications. The dispersion relation is given as follows⁹⁵:

$$R = -\frac{K_m/\epsilon_m}{K_d/\epsilon_d} \quad (4-1a)$$

$$\frac{1-R}{1+R} = \pm e^{-K_d d} \quad (4-1b)$$

where $K_{d,m} = \sqrt{\beta^2 - \omega^2 \epsilon_{d,m}/c^2}$, and β is the propagation constant along y . For convenience we assume the dielectric is air and $\epsilon_d = 1$.

Solving Exact solutions for Eq. (4-1) is difficult. However at the long wavelength limit ($\omega \rightarrow 0$), a solution called symmetric H_z TM mode exists with an approximately linear dispersion law:

$$Re[\beta] = \frac{\omega}{c} \sqrt{\frac{2\lambda_p + d}{d}}, \lambda_p = c/\omega_p \quad (4-2)$$

Usually an antisymmetric mode also is present mathematically but it is ignored as it only exists with a much higher ω (close to ω_p , the plasma frequency of metal).

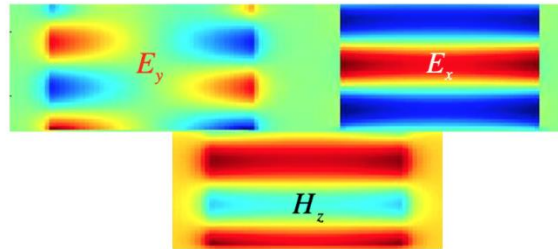


Figure 4-2: Field distribution for the symmetric H_z TM mode.

E_y in the plot has a color scale 1000 times smaller than E_x .

It is worth noting that (still in the subwavelength regime) as $d \gg \lambda_p$, which is typically $\sim 20nm$ for metals like gold, Eq. (4-2) becomes identical to a FEM mode in free space. This is in agreement with our field distribution analysis in the last paragraph. A representative field plot for E_x , E_y and H_z is given in Fig. 4-2.

4.2.2 MDM cavity and its resonance

When the MDM waveguide is truncated in both ends in y , it becomes a cavity. Due to a strong mode mismatch, the propagating TM mode inside MDM excites both reflection and transmission as it hits the truncation interface. It is possible to define a complex reflectivity r to model the reflection of a single TM mode inside MDM. Let's also define the truncation interfaces to be at $y = 0$ on the one side, interfacing with air, and $y = t$ on the other side, interfacing with metal, as it reflects the MDM cavity in our model (Fig. 4-3). It is reasonable to set $r_{y=t} \approx -1$ as most of the field is reflected back. Therefore, we are only left to deal with one remaining parameter $r_{y=0}$.

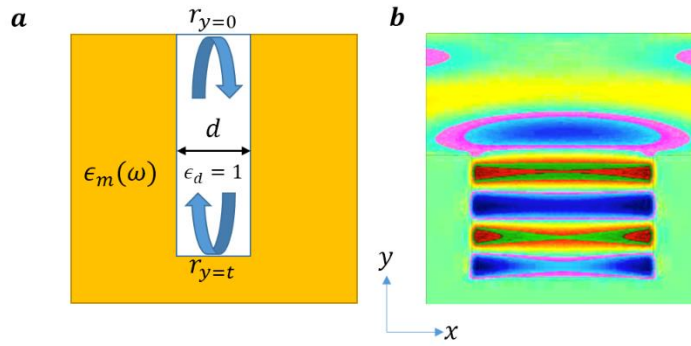


Figure 4-3: A MDM cavity and field distribution E_x at one of its resonance.

The MDM cavity is truncated at $y = 0$ with air and $y = t$ with metal. Complex reflectivity can be defined at these interfaces to model the optical performance of this cavity.

Once cavity is formed, resonances arise so long as for a propagating mode, $Args(r_{y=0}) + Args(r_{y=t}) + 2tRe[\beta] = 2\pi n$. The round trip phase is determined by the propagation constant and reflectivity together. As argued before, $r_{y=t} \approx -1$, so $Args(r_{y=t}) = \pi$. On the other hand, $Re[\beta]$ is known according to Eq. (4-2) given ω . Therefore, the resonance condition of this MDM cavity can be properly modelled if we can solve $r_{y=0}$. Additionally, we can eventually obtain Q factors for a given resonance by Fabry-Perrot models using the formula:

$$Q = \frac{Re[\beta]}{2\alpha - \ln|r_{y=0}|/L} \quad (4-3)$$

where α is the dissipation constant for the guided mode and it is determined by the imaginary part of β as $\alpha = Im[\beta]$.

4.2.3 Reflectivity at the Air-Cavity interface

For a single MDM cavity, by leveraging Fourier transform and continuity of Electrical field as well as Poynting vector at the interface, one can obtain the complex reflectivity $r_{y=0}$ for the symmetric H_z TM in the form of a Fresnel equation⁹⁶:

$$r_{y=0} = \frac{1 - G}{1 + G} \quad (4-4a)$$

$$G = \frac{Z_{MDM}}{Z_0} \frac{1}{2\pi d} \int_{-\infty}^{\infty} \frac{|F(k_x)|^2}{\sqrt{1 - (k_x/k_0)^2}} dk_x \quad (4-4b)$$

$F(k_x)$ is the Fourier coefficient of field profile at $y = 0$ for E_x . k_x is the wave vector in x of plane wave expansion in free space. In the ideal case, E_x can be approximated as a rectangular function with non-zero values only inside the dielectric ($-d/2 \leq x \leq d/2$). Therefore we can write an analytical form for $F(k_x) = sinc(k_x d)$.

Eq. (4-4b) is subject to rich interpretation. In the integral, $k_x > k_0$ represent plane waves to be evanescent in the free space, which does not transport energy. Thus they contribute to the imaginary part of $r_{y=0}$ as $1 - (k_x/k_0)^2 < 0$. On the other hand, $k_x \leq k_0$ waves are exactly the plane waves that take energy to free space from the MDM cavity, making $|r_{y=0}| < 1$.

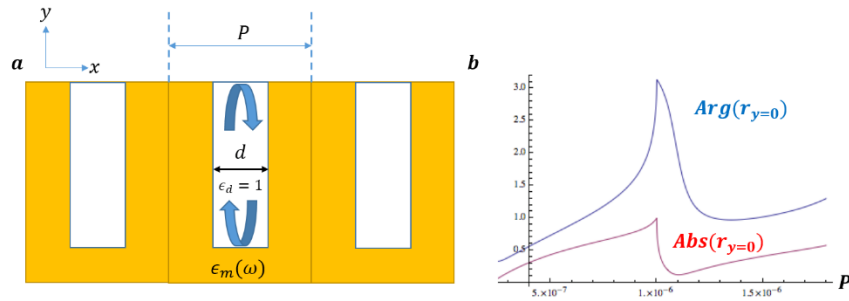


Figure 4-4: MDM cavities in a grating.

a): showing the schematic of a grating with MDM cavities. b): Calculated phase and amplitude of $r_{y=0}$ using formula Eq. (4-5) up to $|m| = 50$.

Eq. (4-4) works well for an isolated MDM cavity interfacing with air. For an array of MDM cavities arranged as a grating (shown in Fig. 4-4), the allowed Floquet modes in free space must have discrete values of k_x , to satisfy the periodic boundary conditions. Specifically, $k_x = \frac{2\pi}{P}m$ where m is an integer and P is the periodicity of the grating. In such cases, Eq. (4-4) replaces its continuous integral with discrete sums as the following:

$$1 + r_{y=0} = \frac{2}{1 + G} \quad (4 - 5a)$$

$$G = \frac{Z_{MDM}}{Z_0} \frac{1}{Pd} \sum_{m=-\infty}^{\infty} \frac{|F(2\pi m \lambda_0 / P)|^2}{\sqrt{1 - (m \lambda_0 / P)^2}} \quad (4 - 5b)$$

The analysis of evanescent and propagating wave contributions to $r_{y=0}$ follows that of Eq. (4-4).

4.2.4 MDM diatomic gratings

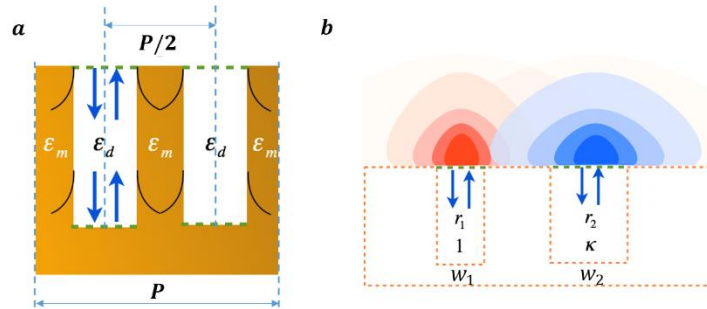


Figure 4-5: Diatomic design for MDM gratings

a): Schematics for a diatomic structure in MDM gratings, with two MDM cavity of slightly different widths w_1, w_2 in one unit cell. They are separated by half the period. b): A “dark mode” emerging from interaction of two MDM cavities the complex ratio of E_x field in right cavity normalized by the left is κ .

We have discussed dark modes and its application in forming high Q overall resonances in chapter 3. It can also be applied to MDM cavity gratings as shown in Fig. 4-5. Let κ be the complex field ratio between two MDM cavities (as one of them is normalized) at steady state. In principle, κ takes two distinct values differing by a phase of π as it is the eigenvalue of a near reflection symmetric system. When $Arg(\kappa) \approx \pi$, it represents a field distribution shown in Fig. 4-5b. The overall reflectivity of the diatomic system reaches minimal and therefore, a high Q resonance mode emerges. The working principles of dark mode mediated high Q resonators have been studied in depths in Chapter 3. Here we will primarily focus on solving r_1 and r_2 for each of the MDM cavities and eventually a r_{eff} for the whole diatomic system.

4.2.5 Coupling between adjacent MDM cavities

Following the unit cell scheme in Fig. 4-5b and let $r_{y=0}$ for the left and right cavity to be r_1 and r_2 respectively. It is possible to calculate r_1 and r_2 simultaneously given κ :

Assuming E_x profiles are rectangular functions at $y = 0$, Eq. (4-5) still holds except that $F(k_x)$ takes in contribution from both cavities:

$$F(k_x) = w_1 \text{Sinc} \left(\frac{w_1 k_x}{2} \right) + \kappa \text{Sinc} \left(\frac{w_2 k_x}{2} \right) e^{-i\pi D k_x} \quad (4-6)$$

where w_1, w_2 are widths for two MDM cavities and D is the size of unit cell. $e^{-i\pi D k_x}$ accounts for a phase shift due to their spatial separation of $D/2$.

Substitute Eq. (4-6) into Eq. (4-5) and solve for r_1, r_2 respectively, we obtain a simultaneous equation:

$$1 + r_1 = \frac{2(1 + w_2 \mathbf{B} - w_2 \kappa \mathbf{D})}{(1 + w_2 \mathbf{B})(1 + w_1 \mathbf{A}) - w_1 w_2 \mathbf{D}^2} \quad (4-7a)$$

$$1 + r_2 = \frac{2 \left(1 + w_1 \mathbf{A} - \frac{w_1 \mathbf{D}}{\kappa} \right)}{(1 + w_2 \mathbf{B})(1 + w_1 \mathbf{A}) - w_1 w_2 \mathbf{D}^2} \quad (4-7b)$$

where \mathbf{A}, \mathbf{B} and \mathbf{D} are complex integrals (sums for a grating) defined as follows:

$$\mathbf{A} = \frac{Z_1}{Z_0 D} \sum_{m=-\infty}^{\infty} \frac{\text{Sinc}^2 \left(\frac{\pi}{D} m w_1 \right)}{\sqrt{1 - (\lambda_0 m / D)^2}} \quad (4-8a)$$

$$\mathbf{B} = \frac{Z_2}{Z_0 D} \sum_{m=-\infty}^{\infty} \frac{\text{Sinc}^2 \left(\frac{\pi}{D} m w_2 \right)}{\sqrt{1 - (\lambda_0 m / D)^2}} \quad (4-8b)$$

$$\mathbf{D} = \frac{\sqrt{Z_1 Z_2}}{Z_0 D} \sum_{m=-\infty}^{\infty} \frac{\text{Sinc} \left(\frac{\pi}{D} m w_2 \right) \text{Sinc} \left(\frac{\pi}{D} m w_1 \right)}{\sqrt{1 - (\lambda_0 m / D)^2}} \quad (4-8c)$$

The symmetric footing of r_1, r_2 is manifest in Eq. (4-7). \mathbf{D} is called the scattering-coupling term as explicit Eq. (4-8), while \mathbf{A}, \mathbf{B} is the self-scattering term. Their physical meaning becomes

apparent when we force to turn off the interaction term, i.e. set $\mathbf{D} = 0$. In such cases, Eq. (4-7) reduces to two independent equations of the exact form of Eq. (4-5), with $G_1 = w_1\mathcal{A}$, $G_2 = w_1\mathcal{B}$ for r_1, r_2 . It is interesting to also note that when $w_1 + w_2 = D$, both cavities get connected hence $\kappa = 1$. It can be shown that as a result, $r_1, r_2 = 0$. This is consistent with the trivial fact both cavities diminish in this case.

r_1, r_2 can be easily solved once we know κ . The problem therefore boils down to getting κ . Unlike special cases discussed above, $\kappa \neq 0$ as the scattering interaction is always present for subwavelength gratings in particular. However we can obtain a set of rules restricting possible values of κ and hope it develops to a self-consistent formula which eventually determines κ together with r_1, r_2 . In a steady state for the diatomic system, we propose the following rules:

1. κ remains a constant for steady state solutions.
2. κ is so that it makes round trip phase differences between to MDM cavities a constant.
3. κ is so that it makes life time for photons in both MDM cavities the same.

Requirement of 1-3 are natural for steady state solutions as both r_1, r_2 depends on κ , and κ comprises of the phase difference and amplitude ratio of fields in the cavities. Point 2-3 essentially explains point 1 with more specificity.

In the context of our MDM models, point 2 and 3 translates to constraints on κ as the following:

$$\text{Args}(r_1) - \text{Args}(r_2) = 2t(\text{Re}[\beta_1] - \text{Re}[\beta_2]) \quad (4 - 9a)$$

$$\frac{\text{Abs}(r_1)}{\text{Abs}(r_2)} = e^{2t(\text{Im}[\beta_1] - \text{Im}[\beta_2])} \quad (4 - 9b)$$

In general, $\text{Re}[\beta_1] \neq \text{Re}[\beta_2]$ as $w_1 \neq w_2$.

However, in the deep subwavelength regime when $w_1, w_2 \gg \lambda_p$, we have $Re[\beta_1] \approx Re[\beta_2]$ by Eq. (4-2). Eq. (4-9a) relaxed to $Args(r_1) = Args(r_2)$. In such cases, κ can be analytically solved to have the form:

$$\kappa_{\pm} = \frac{\mathbf{J} \pm \sqrt{\mathbf{J} + 4w_1w_2\mathbf{D}^2}}{2w_2\mathbf{D}e^{-it\Delta\beta}} \quad (4-10)$$

where $\Delta\beta = \beta_1 - \beta_2$ and \mathbf{J} is again a complex sum in the form of:

$$\mathbf{J} = (1 + w_2\mathbf{B}) - e^{2ti\Delta\beta}(1 + w_1\mathbf{A}) + \frac{(e^{2ti\Delta\beta} - 1)\mathbf{Z}}{2} \quad (4-11a)$$

$$\mathbf{Z} = (1 + w_1\mathbf{A})(1 + w_2\mathbf{B}) - w_1w_2\mathbf{D}^2 \quad (4-11b)$$

D, w_1, w_2 and λ_0 are given, $\mathbf{A}, \mathbf{B}, \mathbf{D}$ are calculated

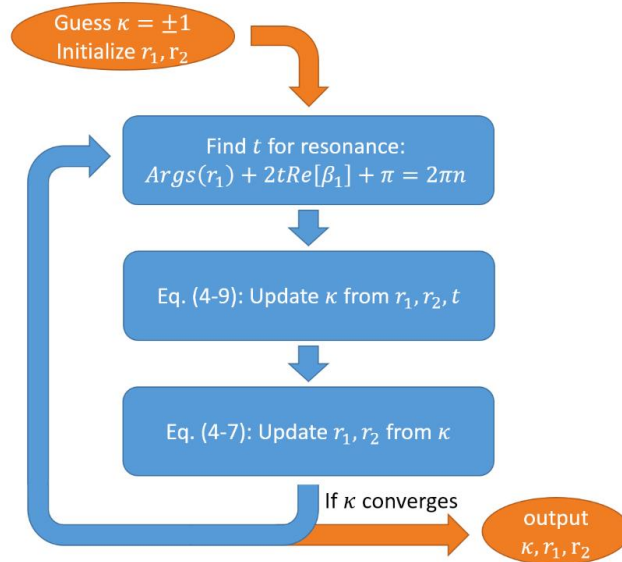


Figure 4-6: An iterative algorithm to calculate κ, r_1, r_2 in a self-consistent way.

The algorithm starts with a naïve guess of $\kappa = \pm 1$, corresponding to bright and dark modes respectively. It then terminates if κ converges after many rounds of updates.

From Eq. (4-10), κ exhibits two solutions of nearly opposite phases. It exactly corresponds to the bright and dark modes of a diatomic system as discussed before.

In the general cases, κ cannot be solved exactly. Therefore, we follow a numerical approach. Note Eq. (4-9a) also depends on t , the depth of MDM cavities. Therefore we develop an iterative method to numerically find self-consistent κ , as depicted in Fig. 4-6. This algorithm is able to find κ, r_1, r_2, t for a given input λ_0 and w_1, w_2, D when the system is at resonance.

4.2.6 Effective Fabry-Perot and Critical Coupling

Once r_1, r_2, κ is obtained, we can alternatively model our diatomic system as an effective Fabry-Perot (F-P) cavity. This can help us understand the resonance condition, Q and talk about round trip phase, overall reflectivity more intuitively. By definition of this terms, and consider the photonic energies in both cavities as a whole, we arrive at the following equations:

$$\left(\frac{\kappa^2(1-r_2^2)}{2t/v_2} + \frac{1-r_1^2}{2t/v_1} \right) / (1+\kappa^2) = \frac{1-r_{eff}^2}{2t/v_{eff}} \quad (4-12a)$$

$$\left(\frac{\kappa^2(1-e^{-4tIm[\beta_2]})}{2t/v_2} + \frac{1-e^{-4tIm[\beta_1]}}{2t/v_1} \right) / (1+\kappa^2) = \frac{1-e^{-4tIm[\beta_{eff}]}}{2t/v_{eff}} \quad (4-12b)$$

$$\frac{\omega/v_{eff}}{2Im[\beta_{eff}] - \ln(r_{eff})/t} = Q \quad (4-12c)$$

where v_i is the phase velocity of light inside each MDM cavity. It can be calculated as $v_i = \omega/Re[\beta_i]$.

Therefore, in principle, our diatomic grating can be effectively modeled as a single F-P cavity. Its resonance shape (presumably Lorentian), position (resonance frequency) and Q factors can be easily predicted using Eq. (4-12) once κ, r_1, r_2, t are solved. The resonance will reach an overall

$R = 0$ when a condition called critical coupling is reached. Physically speaking, it means all photonic energy coupled into the cavity has been absorbed by its round trip loss. By F-P formalism, the condition is given as follows:

$$|r_{eff}| = e^{-2tIm[\beta_{eff}]} \quad (4 - 13)$$

We can use Eq. (4-13) together with Eq. (4-12) to determine the best design for a critically coupled resonator.

4.3 SIMULATION

We run the above algorithm in Mathematica with different combinations of w_2, w_1 and D , for an excitation wavelength of $\lambda_0 = 300\mu m$. $\epsilon_m(\omega)$ is using Drude model of gold. The results are then plotted using Matlab. x, y axes are of μm units.

4.3.1 Q factors of dark modes

Fig. 4-7 is the numerically solved κ in a 2 dimensional parameter space by tuning D and $w_2 - w_1$. As shown in the figure, $Args(\kappa)$ behaves in agreement with our theoretical prediction. Fig. 4-8 further demonstrates how the Q factor differ for bright and dark modes. For the dark mode (using κ_-), Q can be as high as 100 for a metallic resonator; while that of a bright mode lasts around 3 for the whole parameter space we searched.

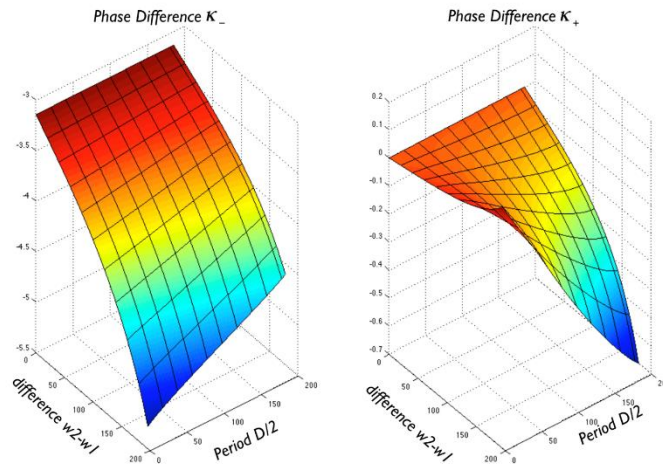


Figure 4-7: Phase of both κ_- and κ_+ in the design parameter space

For smaller $w_2 - w_1$, the dark mode κ has a phase difference close to π , while that of bright κ is close to 0.

It verifies the conclusion we draw in Chapter 3 on dark modes. Because of a π phase difference for the two components in a diatomic structure, its far field radiation is strongly suppressed (thus the name “dark mode”). Therefore, effectively this mode with κ_- enjoys a relatively higher r in the MDM resonator. By Eq. (4-3), this translates to a very large Q resonator given the same intrinsic loss in metallic cavities.

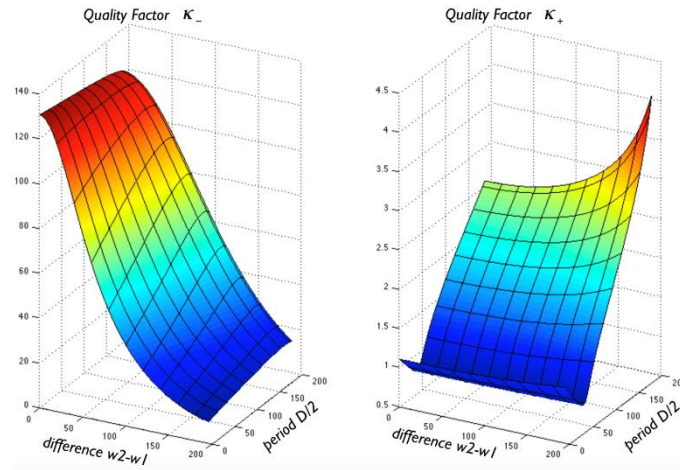


Figure 4-8: Q factors of cavity for both κ_- and κ_+ in the design parameter space.

The dark mode κ has consistently a higher Q than bright modes.

4.3.2 Critically coupling design curves

If we plot $|r_{eff}|$ and $e^{-2tIm[\beta_{eff}]}$ together in the parameter space, as calculated from Eq. (4-12), one can visualize a design curve that satisfies critical coupling.

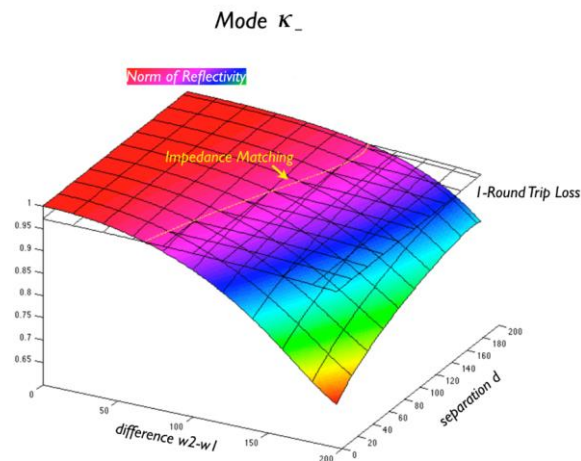


Figure 4-9: Impedance matching design curve.

also known as critically coupling, indicated as a design curve in the parameter space, where the round trip loss surface intercepts the reflectivity amplitude surface.

Critical coupling is a resonance condition when a node in reflection spectrum appears, i.e. $R(\omega_{res}) = 0$. It is also called impedance matching in some literature. Fig. 4-9 demonstrates that our design for dark modes actually support such conditions. The interception of $|r_{eff}|$ and $e^{-2tIm[\beta_{eff}]}$ surfaces forms a line called the critical coupling design curve. Any point in this curve constitutes a dark mode design in diatomic MDM gratings which has $R(\omega_{res}) = 0$. This critical coupling design curve is absent in ordinary bright modes as their $|r_{eff}|$ is much lower than $e^{-2tIm[\beta_{eff}]}$ and thus the two surfaces barely intersect.

4.3.3 An ultra-high Q metallic cavity resonator

We have shown in this chapter that a diatomic MDM cavity gives rise to resonances with an ultra-high Q (up to 50 times higher compared to bright mode ones) thanks to its dark modes.

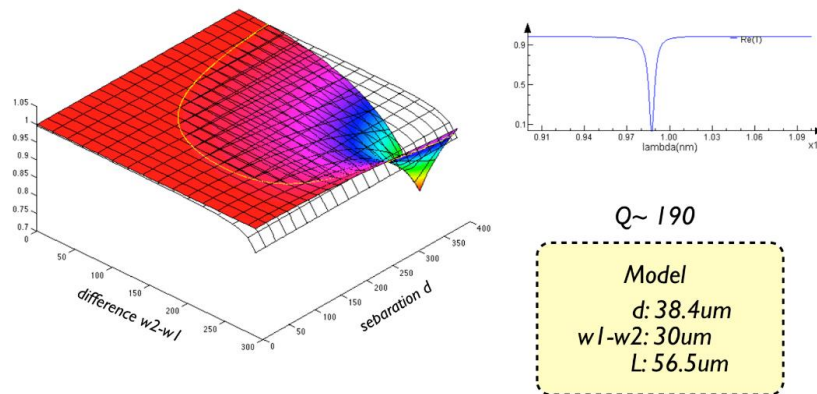


Figure 4-10: A representative diatomic MDM cavity design with critically coupling

It shows a resonance with $Q \sim 190$. The design is confirmed using FDTD calculation. The design parameter is given in the inset box.

We also have shown a numerical algorithm to calculate, given incident wavelength, with what design parameters a high Q dark mode resonance with critical coupling would appear. Here we demonstrate a representative design from our calculation and verify its performance using FDTD

simulation. The result is shown in Fig. 4-10. With a set of design parameters extracted from the design curves, $D = 76.8\mu m$, $t = 56.5\mu m$, $w_2 - w_1 = 30\mu m$, we have achieved a resonance of $Q \sim 190$, centered around $\lambda_{res} = 300\mu m$ (1THz).

4.4 CONCLUSION

We have presented a unique design that achieves high Q in plasmonic resonators by control of its mode reflectivity using a diatomic grating structure. Q factors in those devices are only limited by its intrinsic loss, which is $\frac{Q_{abs}}{2}$ at the critical coupling condition. We have also developed a numerical model that solves the electromagnetism resonance problem in such diatomic MDM cavity gratings. This semi-analytical approach captures the nature of eigensolutions in each cavity and the interaction between them. The model successfully predicts condition for critical coupling as well as Q for those resonances. It can be useful for designing high Q metallic resonators for a variety of applications and its solution lends insight to our understanding towards the high Q modes in diatomic gratings.

REFERENCES

1. Sihvola, A. Metamaterials in electromagnetics. *Metamaterials* **1**, 2–11 (2007).
2. Smith, D. R., Pendry, J. B. & Wiltshire, M. C. K. Metamaterials and Negative Refractive Index. *Sci.* **305**, 788–792 (2004).
3. Schurig, D. *et al.* Metamaterial Electromagnetic Cloak at Microwave Frequencies. *Sci.* **314**, 977–980 (2006).
4. Smith, D. R., Schultz, S., Marko\v{c}i\v{c}, P. & Soukoulis, C. M. Determination of effective permittivity and permeability of metamaterials from reflection and transmission coefficients. *Phys. Rev. B* **65**, 195104 (2002).
5. Linden, S. *et al.* Magnetic Response of Metamaterials at 100 Terahertz. *Sci.* **306**, 1351–1353 (2004).
6. Smith, D. R., Vier, D. C., Koschny, T. & Soukoulis, C. M. Electromagnetic parameter retrieval from inhomogeneous metamaterials. *Phys. Rev. E* **71**, 36617 (2005).
7. Zhang, S. *et al.* Experimental Demonstration of Near-Infrared Negative-Index Metamaterials. *Phys. Rev. Lett.* **95**, 137404 (2005).
8. Shitrit, N. *et al.* Spin-Optical Metamaterial Route to Spin-Controlled Photonics. *Sci.* **340**, 724–726 (2013).
9. Nair, R. R. *et al.* Fine Structure Constant Defines Visual Transparency of Graphene. *Sci.* **320**, 1308 (2008).
10. Das, A. *et al.* Monitoring dopants by Raman scattering in an electrochemically top-gated graphene transistor. *Nat Nano* **3**, 210–215 (2008).
11. Hwang, E. H. & Das Sarma, S. Dielectric function, screening, and plasmons in two-dimensional graphene. *Phys. Rev. B* **75**, 205418 (2007).
12. Ju, L. *et al.* Graphene plasmonics for tunable terahertz metamaterials. *Nat Nano* **6**, 630–634 (2011).

13. Horng, J., Chen, C., Geng, B., Girit, C. & Zhang, Y. Drude conductivity of Dirac fermions in graphene. *Phys. Rev. B* **83**, 165113 (2011).
14. Jin, J.-M. *The finite element method in electromagnetics*. (John Wiley & Sons, 2014).
15. Oskooi, A. F. *et al.* Meep: A flexible free-software package for electromagnetic simulations by the FDTD method. *Comput. Phys. Commun.* **181**, 687–702 (2010).
16. Moharam, M. G., Grann, E. B., Pommet, D. a. & Gaylord, T. K. Formulation for stable and efficient implementation of the rigorous coupled-wave analysis of binary gratings. *J. Opt. Soc. Am. A* **12**, 1068 (1995).
17. Taflove, A., Hagness, S. C. & others. Computational electrodynamics: the finite-difference time-domain method. *Norwood, 2nd Ed. MA Artech House, 1995* (1995).
18. Kunz, K. S. & Luebbers, R. J. *The finite difference time domain method for electromagnetics*. (CRC press, 1993).
19. Kane Yee. Numerical solution of initial boundary value problems involving maxwell's equations in isotropic media. *IEEE Trans. Antennas Propag.* **14**, 302–307 (1966).
20. Sullivan, D. M. Frequency-dependent FDTD methods using Z transforms. *IEEE Trans. Antennas Propag.* **40**, 1223–1230 (1992).
21. Berenger, J.-P. A perfectly matched layer for the absorption of electromagnetic waves. *J. Comput. Phys.* **114**, 185–200 (1994).
22. Peng, S. T. Rigorous formulation of scattering and guidance by dielectric grating waveguides: general case of oblique incidence. *J. Opt. Soc. Am. A* **6**, 1869–1883 (1989).
23. Moharam, M. & Gaylord, T. Rigorous coupled-wave analysis of planar-grating diffraction. *JOSA* **71**, 811–818 (1981).
24. Ferguson, B. & Zhang, X.-C. Materials for terahertz science and technology. *Nat. Mater.* **1**, 26–33 (2002).

25. Williams, G. P. Filling the THz gap—high power sources and applications. *Reports Prog. Phys.* **69**, 301–326 (2006).
26. Sirtori, C., Barbieri, S. & Colombelli, R. Wave engineering with THz quantum cascade lasers. *Nat. Photonics* **7**, 691–701 (2013).
27. Welp, U., Kadowaki, K. & Kleiner, R. Superconducting emitters of THz radiation. *Nat. Photonics* **7**, 702–710 (2013).
28. Dai, J., Xie, X. & Zhang, X.-C. Detection of Broadband Terahertz Waves with a Laser-Induced Plasma in Gases. *Phys. Rev. Lett.* **97**, 103903 (2006).
29. Vicarelli, L. *et al.* Graphene field-effect transistors as room-temperature terahertz detectors. *Nat Mater* **11**, 865–871 (2012).
30. Sensale-Rodriguez, B. *et al.* Broadband graphene terahertz modulators enabled by intraband transitions. *Nat. Commun.* **3**, 780 (2012).
31. Lee, S. H. *et al.* Switching terahertz waves with gate-controlled active graphene metamaterials. *Nat. Mater.* **11**, 936–41 (2012).
32. Valmorra, F. *et al.* Low-Bias Active Control of Terahertz Waves by Coupling Large-Area. *Nano Lett.* **13**, 3193–3198 (2013).
33. Schuller, J. a *et al.* Plasmonics for extreme light concentration and manipulation. *Nat. Mater.* **9**, 193–204 (2010).
34. Maier, S. & Atwater, H. Plasmonics: Localization and guiding of electromagnetic energy in metal/dielectric structures. *J. Appl. Phys.* **98**, 011101 (2005).
35. Alu, A. & Engheta, N. Tuning the scattering response of optical nanoantennas with nanocircuit loads. *Nat Phot.* **2**, 307–310 (2008).
36. Alù, A. & Engheta, N. Tuning the scattering response of optical nanoantennas with nanocircuit loads. *Nat. Photonics* **2**, 307–310 (2008).
37. Chen, H.-T. *et al.* Active terahertz metamaterial devices. *Nature* **444**, 597–600 (2006).

38. Lee, S. H. *et al.* Broadband Modulation of Terahertz Waves With Non-Resonant Graphene Meta-Devices. *IEEE Trans. terzhertz Sci. Technol.* **3**, 764–771 (2013).
39. Seo, M. A. *et al.* Terahertz field enhancement by a metallic nano slit operating beyond the skin-depth limit. *Nat. Photonics* **3**, 152 (2009).
40. Kang, J., Kim, D. & Park, Q.-H. Local Capacitor Model for Plasmonic Electric Field Enhancement. *Phys. Rev. Lett.* **102**, 093906 (2009).
41. Novitsky, A. *et al.* Non-resonant terahertz field enhancement in periodically arranged nanoslits. *J. Appl. Phys.* **112**, 074318 (2012).
42. Horng, J. *et al.* Drude conductivity of Dirac fermions in graphene. *Phys. Rev. B* **83**, 165113 (2011).
43. Ren, L. *et al.* Terahertz and infrared spectroscopy of gated large-area graphene. *Nano Lett.* **12**, 3711–5 (2012).
44. Tan, Y.-W. *et al.* Measurement of Scattering Rate and Minimum Conductivity in Graphene. *Phys. Rev. Lett.* **99**, 246803 (2007).
45. Li, X. *et al.* Large-area synthesis of high-quality and uniform graphene films on copper foils. *Science* **324**, 1312–4 (2009).
46. Shi, S.-F. *et al.* Controlling graphene ultrafast hot carrier response from metal-like to semiconductor-like by electrostatic gating. *Nano Lett.* **14**, 1578–82 (2014).
47. Kim, B. J. *et al.* High-performance flexible graphene field effect transistors with ion gel gate dielectrics. *Nano Lett.* **10**, 3464–6 (2010).
48. El Beheiry, M., Liu, V., Fan, S. & Levi, O. Sensitivity enhancement in photonic crystal slab biosensors. *Opt. Express* **18**, 22702–14 (2010).
49. Shi, L., Pottier, P., Peter, Y.-A. & Skorobogatiy, M. Guided-mode resonance photonic crystal slab sensors based on bead monolayer geometry. *Opt. Express* **16**, 17962 (2008).
50. Suh, W., Yanik, M. F., Solgaard, O. & Fan, S. Displacement-sensitive photonic crystal structures based on guided resonance in photonic crystal slabs. *Appl. Phys. Lett.* **82**, 1999

- (2003).
51. Magnusson, R. & Wang, S. S. New principle for optical filters. *Appl. Phys. Lett.* **61**, 1022 (1992).
 52. Peng, S. & Morris, G. M. Resonant scattering from two-dimensional gratings. *J. Opt. Soc. Am. A* **13**, 993 (1996).
 53. Tibuleac, S. & Magnusson, R. Reflection and transmission guided-mode resonance filters. *J. Opt. Soc. Am. A* **14**, 1617 (1997).
 54. Wang, S. S. & Magnusson, R. Theory and applications of guided-mode resonance filters. *Appl. Opt.* **32**, 2606–13 (1993).
 55. Wang, Q. *et al.* Colored image produced with guided-mode resonance filter array. *Opt. Lett.* **36**, 4698–700 (2011).
 56. Cho, E.-H. *et al.* Nanoimprinted photonic crystal color filters for solar-powered reflective displays. *Opt. Express* **18**, 27712–22 (2010).
 57. Boroditsky, M. *et al.* Light extraction from optically pumped light-emitting diode by thin-slab photonic crystals. *Appl. Phys. Lett.* **75**, 1036 (1999).
 58. Mekis, A., Dodabalapur, a., Slusher, R. E. & Joannopoulos, J. D. Two-dimensional photonic crystal couplers for unidirectional light output. *Opt. Lett.* **25**, 942 (2000).
 59. Lu, T.-C. *et al.* GaN-based two-dimensional surface-emitting photonic crystal lasers with AlN/GaN distributed Bragg reflector. *Appl. Phys. Lett.* **92**, 011129 (2008).
 60. Fattal, D., Li, J., Peng, Z., Fiorentino, M. & Beausoleil, R. G. Flat dielectric grating reflectors with focusing abilities. *Nat. Photonics* **4**, 466–470 (2010).
 61. Yu, N. & Capasso, F. Flat optics with designer metasurfaces. *Nat. Mater.* **13**, 139–50 (2014).
 62. Joannopoulos, J. D., Villeneuve, P. R. & Fan, S. Photonic crystals: putting a new twist on light. *Nature* **386**, 143–149 (1997).

63. Slabs, P. C., Asano, T., Song, B., Akahane, Y. & Noda, S. Ultrahigh- Q Nanocavities in Two-Dimensional. **12**, 1123–1134 (2006).
64. Briggs, C., Buxkemper, T., Czaia, L., Green, H. & Gustafson, S. Ultra-high- Q toroid microcavity on a chip. **421**, 925–928 (2003).
65. Niehusmann, J., Vörckel, A., Bolivar, P. H., Wahlbrink, T. & Henschel, W. microring resonator. **29**, 2861–2863 (2004).
66. Chow, E., Grot, a., Mirkarimi, L. W., Sigalas, M. & Girolami, G. Ultracompact biochemical sensor built with two-dimensional photonic crystal microcavity. *Opt. Lett.* **29**, 1093 (2004).
67. Fan, S. & Joannopoulos, J. Analysis of guided resonances in photonic crystal slabs. *Phys. Rev. B* **65**, 235112 (2002).
68. Yao, Y. *et al.* Broad electrical tuning of graphene-loaded plasmonic antennas. *Nano Lett.* **13**, 1257–64 (2013).
69. Wang, S. S. & Magnusson, R. Design of waveguide-grating filters with symmetrical line shapes and low sidebands. *Opt. Lett.* **19**, 919 (1994).
70. Karagodsky, V. & Chang-Hasnain, C. J. Physics of near-wavelength high contrast gratings. *Opt. Express* **20**, 10888–95 (2012).
71. Wang, S. S. & Magnusson, R. Multilayer waveguide-grating filters. *Appl. Opt.* **34**, 2414–20 (1995).
72. Sharon, a., Rosenblatt, D. & Friesem, a. a. Narrow spectral bandwidths with grating waveguide structures. *Appl. Phys. Lett.* **69**, 4154 (1996).
73. Zhang, S., Genov, D. a., Wang, Y., Liu, M. & Zhang, X. Plasmon-Induced Transparency in Metamaterials. *Phys. Rev. Lett.* **101**, 047401 (2008).
74. Stockman, M. I., Faleev, S. V & Bergman, D. J. Localization versus Delocalization of Surface Plasmons in Nanosystems: Can One State Have Both Characteristics? *Phys. Rev. Lett.* **87**, 167401 (2001).

75. Luk'yanchuk, B. *et al.* The Fano resonance in plasmonic nanostructures and metamaterials. *Nat. Mater.* **9**, 707–15 (2010).
76. Verellen, N. *et al.* Fano resonances in individual coherent plasmonic nanocavities. *Nano Lett.* **9**, 1663–7 (2009).
77. Liu, N. *et al.* Plasmonic analogue of electromagnetically induced transparency at the Drude damping limit. *Nat. Mater.* **8**, 758–62 (2009).
78. Karagodsky, V., Sedgwick, F. G. & Chang-Hasnain, C. J. Theoretical analysis of subwavelength high contrast grating reflectors. *Opt. Express* **18**, 16973–88 (2010).
79. Chandran, A., Barnard, E. S., White, J. S. & Brongersma, M. L. Metal-dielectric-metal surface plasmon-polariton resonators. *Phys. Rev. B* **85**, 85416 (2012).
80. Ochiai, T. & Sakoda, K. Dispersion relation and optical transmittance of a hexagonal photonic crystal slab. *Phys. Rev. B* **63**, 125107 (2001).
81. Lemarchand, F., Sentenac, a. & Giovannini, H. Increasing the angular tolerance of resonant grating filters with doubly periodic structures. *Opt. Lett.* **23**, 1149 (1998).
82. Fehrembach, A.-L., Talneau, A., Boyko, O., Lemarchand, F. & Sentenac, A. Experimental demonstration of a narrowband, angular tolerant, polarization independent, doubly periodic resonant grating filter. *Opt. Lett.* **32**, 2269 (2007).
83. Lemarchand, F., Sentenac, a, Cambril, E. & Giovannini, H. Study of the resonant behaviour of waveguide gratings: increasing the angular tolerance of guided-mode filters. *J. Opt. A Pure Appl. Opt.* **1**, 545–551 (1999).
84. Mizutani, A., Kikuta, H. & Iwata, K. Wave Localization of Doubly Periodic Guided-mode Resonant Grating Filters. *Opt. Rev.* **10**, 13–18 (2003).
85. Zengerle, R. Light Propagation in Singly and Doubly Periodic Planar Waveguides. *J. Mod. Opt.* **34**, 1589–1617 (1987).
86. Fan, S., Suh, W. & Joannopoulos, J. D. Temporal coupled-mode theory for the Fano resonance in optical resonators. *J. Opt. Soc. Am. A* **20**, 569–572 (2003).

87. Liu, N., Mesch, M., Weiss, T., Hentschel, M. & Giessen, H. Infrared perfect absorber and its application as plasmonic sensor. *Nano Lett.* **10**, 2342–8 (2010).
88. Wang, F. & Shen, Y. General Properties of Local Plasmons in Metal Nanostructures. *Phys. Rev. Lett.* **97**, 206806 (2006).
89. Magnusson, R. & Shokooch-Saremi, M. Widely tunable guided-mode resonance nanoelectromechanical RGB pixels. *Opt. Express* **15**, 10903–10910 (2007).
90. Kauranen, M. & Zayats, A. V. Nonlinear plasmonics. *Nat. Photonics* **6**, 737–748 (2012).
91. Gramotnev, D. K. & Bozhevolnyi, S. I. Plasmonics beyond the diffraction limit. *Nat. Photonics* **4**, 83–91 (2010).
92. Zeng, B., Majumdar, A. & Wang, F. Tunable dark modes in one-dimensional ‘diatomic’ dielectric gratings. *Opt. Express* **23**, 12478–87 (2015).
93. Martín-Moreno, L. *et al.* Theory of Extraordinary Optical Transmission through Subwavelength Hole Arrays. *Phys. Rev. Lett.* **86**, 1114–1117 (2001).
94. Ebbesen, T. W., Lezec, H. J., Ghaemi, H. F., Thio, T. & Wolff, P. A. Extraordinary optical transmission through sub-wavelength hole arrays. **391**, 667–669 (1998).
95. Economou, E. N. Surface Plasmons in Thin Films. *Phys. Rev.* **182**, 539–554 (1969).
96. Gordon, R. Light in a subwavelength slit in a metal: Propagation and reflection. *Phys. Rev. B* **73**, 153405 (2006).